Experimental and numerical study of cavitating flow around a surface mounted semi-circular cylinder

Ghahramani, Ebrahim; Jahangir, Saad; Neuhauser, Magdalena; Bourgeois, Sébastien; Poelma, Christian; Bensow, Rickard E.

DOI
10.1016/j.ijmultiphaseflow.2019.103191

Publication date
2020

Document Version
Final published version

Published in
International Journal of Multiphase Flow

International Journal of Multiphase Flow 124 (2020) 103191

Contents lists available at ScienceDirect

International Journal of Multiphase Flow

journal homepage: www.elsevier.com/locate/ijmulflow

Experimental and numerical study of cavitating flow around a surface mounted semi-circular cylinder

Ebrahim Ghahramani[a,*], Saad Jahangir[b], Magdalena Neuhauser[c], Sébastien Bourgeois[c], Christian Poelma[b], Rickard E. Bensow[a]

[a] Mechanics and Maritime Sciences, Chalmers University of Technology, Gothenburg, 412 96, Sweden
[b] Department of Process & Energy (Faculty 3mE), Delft University of Technology, 2628 CA Delft, The Netherlands
[c] R&D Department, ANDRITZ Hydro, Vevey 1800, Switzerland

ARTICLE INFO

Article history:
Received 19 June 2019
Revised 1 November 2019
Accepted 21 December 2019
Available online 23 December 2019

Keywords:
Cavitation
Bluff body
High speed imaging
Multiphase flow

ABSTRACT

In this paper, the cavitating flow around a bluff body is studied both experimentally and numerically. The bluff body has a finite length with semi-circular cross section and is mounted on a surface in the throat of a converging-diverging channel. This set-up creates various 3D flow structures around the body, from cavitation inception to super cavities, at high Reynolds numbers ($Re = 5.6 \times 10^4 - 2.2 \times 10^5$) and low cavitation numbers ($\sigma = 0.56 - 1.69$). Earlier studies have shown this flow to be erosive and the erosion pattern varies by changing the flow rate and w/o the cylinder; hence, this study is an attempt to understand different features of the cavitating flow due to the cylinder effect. In the experiments, high-speed imaging is used. Two of the test cases are investigated in more detail through numerical simulations using a homogeneous mixture model. Non-cavitating simulations have also been performed to study the effect of cavitation on the flow field. Based on the observed results, vortex shedding can have different patterns in cavitating flows. While at higher cavitation numbers the vortices are shed in a cyclic pattern, at very low cavitation numbers large fixed cavities are formed in the wake area. For mid-range cavitation numbers a transitional regime is seen in the shedding process. In addition, the vapour structures have a small effect on the flow behaviour for high cavitation numbers, while at lower cavitation numbers they have significant influence on the exerted forces on the bluff body as well as vortical structures and shedding mechanisms. Besides, at very low cavitation numbers, a reverse flow is observed that moves upstream and causes the detachment of the whole cavity from the cylinder. Such a disturbance is not seen in non-cavitating flows.

1. Introduction

Cavitation is a phenomenon in which liquid is converted into vapour due to the local drop of fluid pressure below the vapour pressure. It is a common and mostly undesirable event in hydraulic systems such as pumps, turbines and ship propellers. Cavitation can cause noise, load variations, blockage in the machinery and system vibrations which may lead to fatigue failure (Balas et al., 2006; Van Terwisga, 2009). Also, cavitation erosion may lead to material loss and degradation of the system. However, it is a desirable event in some other situations such as ultrasonic cleaning and ultrasonic drug delivery (Ibsen et al., 2013) and mixing two or more dissimilar fluids such as in marine diesel engines (Avellan et al., 1991; Habchi et al., 2014). Therefore, understanding the cavitation physics is of considerable importance for reliable prediction and control of its occurrence in the design of hydraulic and marine systems as well as its application in biomedical treatment and chemical systems.

For this purpose, various experimental and numerical studies have been performed on simpler geometries and benchmark test cases to recognize different flow characteristics and parameters that lead to abrupt pressure drop, cavity generation and its violent collapse. Three types of flow geometries are used frequently as they can be more representative of different fundamental cavitation patterns. They include (1) flow over lifting bodies (e.g. Foeth et al., 2008; Asnaghi et al., 2017) in which the pressure drop on the suction side is the major cause of cavitation; (2) liquid flow inside converging-diverging nozzles (e.g. Jahangir et al., 2018; Ganesh et al., 2016) where the variations in flow area leads to considerable variations of velocity and pressure magnitudes, which may be accompanied by various cavity patterns (Jahangir et al., 2018); and

* Corresponding author.
E-mail address: ebrahim.ghahramani@chalmers.se (E. Ghahramani).

https://doi.org/10.1016/j.ijmultiphaseflow.2019.103191
0301-9322/

(3) flow around bluff bodies in which the low pressure wake region is susceptible to cavity generation. As compared to the first two groups, the flow around a bluff body is generally more periodic which makes the measurements more reproducible. Besides that, in similar testing conditions, cavity structures around a bluff body can be considerably more aggressive and more erosive. The work of Escaler et al. (2003), for example, shows that mounting a small bluff body on a hydrofoil induces severe localised erosion, where cavities collapse on a narrow region in the wake of the bluff body.

The characteristics of the cavitation around a bluff body can be highly dependent on the shape of the body. The flow around a circular cylinder has been the subject of various studies in literature for both cavitating and non-cavitating conditions as it has broad engineering applications. Matsudaira et al. (1992) studied the flow pattern in a cavitating von Kármán vortex street behind a circular cylinder for different Reynolds and cavitation numbers and found that the bubbles frequently collapse when the von Kármán vortex separates from the cylinder or the attached cavity. By investigating the cavitation collapse and impact behind a circular cylinder, Saito and Sato (2003) observed that the von Kármán vortex cavities are divided into different parts and the structures located near the channel wall collapses rapidly with a colliding motion towards the wall. Also, it was seen that the collapses have three different patterns, namely: 3D-radial collapse, 2D-radial collapse and axial collapse. Gnanaskandan and Mahesh (2016) performed a detailed numerical investigation on the effect of cavitation on the near-wake characteristics of flow over circular cylinder. According to their study, cavitation influences the evolution of the boundary layer and loads on the cylinder surface. In particular, the vortex shedding Strouhal number decreases as the flow cavitates, which was shown to be mainly due to vorticity dilatation. It was also observed that at lower cavitation numbers, the entire vapour cavity detaches from the cylinder at low frequencies, which was concluded to occur due to a propagating condensation front. The reduction in vortex shedding frequency is further seen in the experimental and numerical studies of Kumar et al. (2017, 2018). In these studies, it was observed that reductions in pressure and turbulent kinetic energy are accompanied by an increase in vapour volume fraction during the vaporization stage, while a collapse in the vapour volume accompanies pressure and turbulent energy increases. Moreover, there are a number of studies that show that cavitation influences the generated noise by the cylindrical obstacle (e.g. Rao and Chandrasekhara, 1976; Fry, 1984; Seo et al., 2008). Aside from circular cylinders, there are some studies which have been performed on other geometries. Brandner et al. (2010) experimentally investigated cavitating flow over a sphere at a high Reynolds number of 1.5×10^6 and for cavitation numbers of 0.36 to 1. According to this study, the boundary layer at cavity separation is laminar for different cavitation numbers. Also, at intermediate cavitation numbers, a re-entrant jet develops which leads to shedding of large-scale von Kármán vortices. Young and Holl (1966) studied the cavitation effects on the flow in the wake of triangular bluff bodies, nominally two-dimensional wedges, with different apex angles. Contrary to the circular cylinder case, it was observed that when the cavitation number is below half of the cavitation inception number, the Strouhal number increases for a decreasing cavitation number. However, after reaching a peak value, the Strouhal number decreases again by further reducing the cavitation number. The same behaviour is seen in the recent study of Ganesh et al. (2018)

Another special type of bluff bodies that is of particular interest, is the semi-circular cylinder. A major difference between a flat front semi-circular obstacle and other types of bluff bodies discussed earlier is that with semi-circular section the flow separates from the cylinder edges as it hits the obstacle, while in other cases a boundary layer area develops on the forebody part, and prior to separation and cavitation inception the flow is attached to the body surface and in the particular case of the sphere, a re-entrant jet can develop that leads to shedding of cavitating vortices, as stated above. Yamagata et al. (2015) studied the Aeolian tone (sound generated by flow over objects) from a semi-circular cylinder in a uniform flow at different angle of attacks and compared the results with a circular cylinder. According to this study, the wake width in the transverse direction for the flat front semi-circular body is $1.7D$ which is considerably wider than circular and flat back semi-circular bodies ($width \approx 1.1D$), and it can be explained due to the flow separation at the cylinder edges. Also, the flat front semi-circular case had the highest sound pressure level as compared to other angle of attacks and its corresponding Strouhal number ($St = 0.12$) was lower than any other body orientation and the circular case ($St = 0.19$), which can be related to its wake width (Yamagata et al., 2015). When facing the flow with their flat surface, semi-circular cylinders can significantly increase the flow erosiveness. While it is usually tried to avoid cavitation erosion in engineering applications, the bluff bodies can be used in the resistance test of different materials and coatings as they accelerate the erosion process and it is of particular importance to understand possible sources of their erosiveness. In an experimental work, Escaler et al. (2001) mounted semi-circular obstacles on the suction side of a hydrofoil to alter the flow field in order to accelerate the erosion process. They had tested four different obstacles and found the semi-circular cross section to be the most adequate geometry for generating reproducible pitting on the specimen within a short period of time. In another study by the same group (Escaler et al., 2003), it is observed that such an obstacle induces severe localised erosion by the collapse of strong cavitation vortices on a narrow region. Besides that, earlier studies at Andritz Hydro have shown that the flow behind the semi-circular cylinder can be quite erosive and the erosion pattern varies both by changing the flow rate and by including/removing the cylinder in the set-up. Hence, in the current study different cavitation regimes behind a semi-circular cylinder are investigated to understand various flow features around sharp edged bluff bodies. Studies analysing the cavity structure behind semi-circular bodies have not been published previously. In a recent study, Wang et al. (2018) investigated ventilated cavitating flow behind a similar geometry with various gas entertainment rates. However, the obtained cavity structures in that study have considerable differences with the non-ventilated case, as will be depicted in the current paper.

The objective of this study is to analyse the cavitating flow around a semi-circular cylindrical obstacle. Over the years many non-intrusive experimental techniques have been developed to investigate cavitating flows. These techniques include high-speed visualization, X-ray densitometry (e.g. Mitroglou et al., 2016; Dash et al., 2018; Jahangir et al., 2019) and magnetic resonance velocimetry (e.g. Adair et al., 2018), with each technique having its benefits and drawbacks. High-speed visualization is the most popular technique to investigate the cavitation evolution due to its unsurpassed temporal resolution. This technique helps in capturing in detail the transient flow behavior. In this study, we use high-speed visualization to analyse this complex cavitating flow. We consider different cavitation numbers to investigate various structures from small inception bubbles at high cavitation numbers to super cavities at very low ones. The experimental tests have been performed using the cavitation test rig in the ANDRITZ Hydraulic Laboratory. To investigate more flow details that are not easily detectable from experiments, two of the test cases are simulated numerically as well. The most common cavitation models that are used in literature are the homogeneous mixture models, which can be categorized into equilibrium models (e.g. Schnerr et al., 2008; Eskilsson and Bensow, 2012) and transport equation based

models (e.g. Singhal et al., 2002; Bensow and Bark, 2010). Also, some hybrid Eulerian-Lagrangian models have been developed in recent years (e.g. Ghahramani et al., 2018). A detailed description of different numerical models can be found in the work of Ghahramani et al. (2019). In this study a transport equation based finite mass model is used which has been shown to give satisfactory results with reasonable computational cost in earlier studies (Asnaghi et al., 2015; Asnaghi et al., 2018; Schenke and van Terwisga, 2019). The simulations are performed using the open source C++ package OpenFOAM-2.2.x (OpenFoam, 2013).

In the following sections, the test facility and experimental conditions are described first. After that, the experimental method and data processing are explained which is followed by a short description of the numerical model and simulation setup. Then, the obtained results are presented in detail, including a discussion about different flow structures, cavity inception, the cavitation effect on the flow field, etc. Finally, the paper is concluded with recommendations for future studies.

2. Methodology

2.1. Experimental details

A schematic overview of the flow setup utilized for the experiments is represented in Fig. 1(a). The flow in the loop system is driven by a pump (KSB 6N89-858-233) from an open water tank, which is installed approximately 1.98 m below the main feeding line to avoid cavitation in the pump. An electromagnetic flowmeter (DN 100 from ABB) is used to measure the volumetric flow rate. An enlarged view of the test section is shown in Fig. 1(b). To have a larger pressure drop and higher local velocities, which augments cavitation, the channel has a converging-diverging rectangular cross section with dimensions of 74×54 mm^2 which is contracted to a section of 25×54 mm^2 through a curved profile upper wall and a simple 45° slope on the lower wall, while the channel width is constant everywhere. The bluff body is put at the end of the lower slope and after that, there is a flat plate with dimension of 106×54 mm^2. The flat side of the cylinder is facing upstream and at the attachment of the flat plate and the sloped wall, there is small backward facing step with a height of 0.5 mm. The upstream length available for development is more than 100D, in order to have a fully-developed turbulent flow entering the test section. The feeding line of the experimental setup is a circular tube with a diameter of 114.3 mm, however it is transformed to a rectangular section (74×54 mm^2) through a converging tube at 140 cm before the main test section. After the test section, the pressure in the flow is recovered in a pressure recovery section, with an overall length of 2.4 m. At the end of the pressure recovery section, a valve is present to vary the global static pressure of the system. There are two outflow pipes, however only the second pipe is used during the tests. The first pipe is just for maintenance purpose and emptying the test rig. The flow can be visualized through the side walls, which are made of Polymethyl methacrylate (PMMA). Also, two pressure transducers are used to measure the upstream (p_1) and downstream pressure (p_2), which are located 379.5 mm before and 500.5 mm after the bluff body, respectively.

The bluff body is a flat-front semi-circular cylinder with a diameter of 5 mm and a height of 9.65 mm (red cylinder in Fig. 1(b)). Cavitation was achieved by increasing the flow speed at the throat while the pressure is the same at the inlet tank. Controlling the cavitation number in this way (changing flow speed) affects the Reynolds number (and thus possibly the turbulence statistics). This is due to the design of the facility, which does not allow control over the pressure separately. Here we only use high speed visualization, which does not allow measurement of flow turbulence levels. However, it is assumed that the flow behaviour does not vary considerably due to turbulence effect for the investigated range of Reynolds number ($Re = 7.4 \times 10^4 - 21.5 \times 10^4$) for bluff bodies with separation at sharp edges. Such an assumption can be verified later in the numerical drag coefficients of non-cavitating flows (Fig. 24). The measurements from the downstream pressure transducer (Rosemount differential pressure transducer, Model: 3051S1D), the flowmeter, and the temperature sensor are used to determine the cavitation number σ. Throughout the paper, the flow conditions will be reported based on the cavitation number:

$$\sigma = \frac{p_2 - p_v}{\frac{1}{2}\rho u_{th}^2}, \tag{1}$$

where p_2 is the downstream pressure, p_v is the vapor pressure[1], ρ is the density of the liquid and u_{th} is the area-averaged velocity of the flow at the throat of the converging-diverging section without cylinder. The fluid temperature had negligible variation between 20.59 °C and 20.67 °C through the whole experiment.

2.2. Experimental procedure

Before the measurements, a water sample was attained for the determination of the oxygen content in the system using an oxygen sensor (RDO PRO-X Probe). The experimental setup was run for a few minutes before the measurement series is commenced. It helps in mixing the water in the system to obtain a uniform water temperature. The flow was achieved by changing the flow rate using the pump and this in turn imposes a pressure difference ($p_1 - p_2$) over the section. For each case, the flow rate is set to a designated value and the measurements are started when the pressure measurements are stable. All the sensor values (pressure, flow rate, and temperature) and high-speed images (explained in more detail in the next paragraph) were stored simultaneously, utilizing a data acquisition system. After performing a measurement, the flow velocity was decreased. In the end, the oxygen content was determined again by attaining a water sample from the setup. As the volume of tank was large no difference was seen in the oxygen measurements. The average dissolved oxygen content was 8.25 mg/L with negligible variation through the whole series of experiment.

2.3. High-speed imaging

The cavity dynamics are captured using high-speed imaging. A picture of the set-up is shown in Fig. 2. In these measurements, three light sources were used. A homogeneous light source, a LED panel, is placed behind the measurement section. This light source illuminates the target from the back side in the direction of the CMOS camera sensor. Two light sources illuminate the front side of the cavity. The measurement target is placed between the light sources and a high-speed camera. In this way, the presence and position of vapor cavities can be determined. As the refractive index of PMMA (1.49) is relatively close to water (1.33), the high-speed images were not distorted significantly due to refraction. We used the known length of the flat plate behind the body to measure the cavity length. The plate and cavity lengths were measured in the same plane. In this way, the difference in the refraction does not cause any error. Two different lighting conditions were used in order to understand the cavitation structures better for different cavitation numbers. For light condition LC1, the recordings were performed with all the three illuminations turned on, while for condition LC2, only the back illumination source was turned on.

[1] The vapor pressure is calculated using the Antoine equation at measured the temperature.

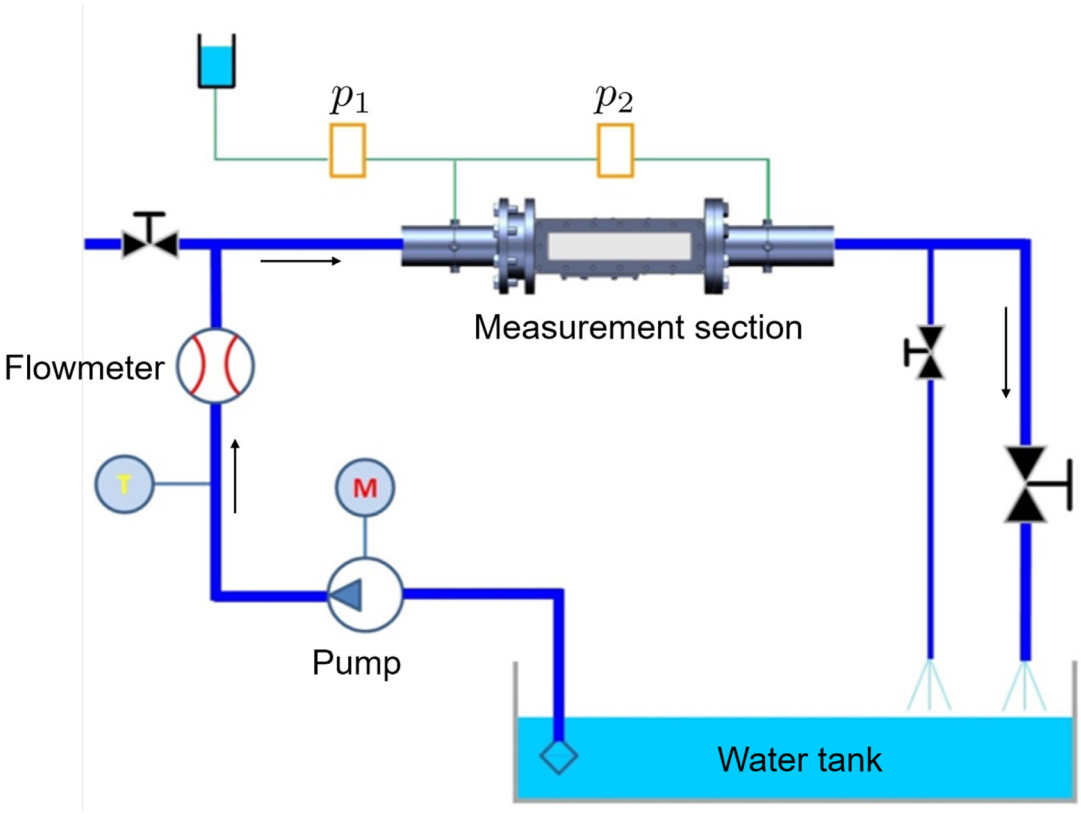

(a)

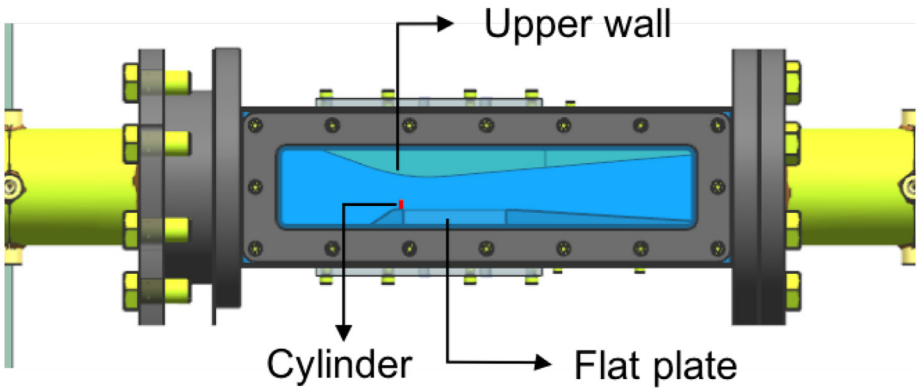

(b)

Fig. 1. (a) Schematic overview of the experimental facility indicating different components; (b) Enlarged view of the test section (dimensions not to scale).

A high-speed camera (Phantom v411) in combination with a 20–50 mm/3.3 MACRO-NIKKOR object-glass is adapted for recording. For the experiments an aperture $f^{\#}$=3.3 was set as well as a field of view of 640 $\times$ 232 pixels. For the experiments, two different positions of the camera were used: one parallel to the measurement section which we call "side view" and the other one at 32° to the measurements section that we call "inclined top view". An exposure time of 39 µs is used in combination with a frame rate of 25000 Hz ($\Delta T = 4 \times 10^{-5}$ sec) and a recording time of 0.25 s for each measurement. The recorded videos are used for the determination of the cavity shedding frequency and cavity length.

2.4. Numerical method

In this study we investigate the cavitating flow behind a bluff body and over a flat surface, in which the cavities may grow to the whole length of the surface. The most commonly used numerical model at such length scale, is the homogeneous mixture model. In the simulations, we use a transport equation based, homogeneous mixture model that treats the vapour and liquid phases as a single mixture fluid, and the continuity equation and one set of momentum equations for the mixture are solved. Also, the liquid-vapour mixture is represented by solving a scalar transport equa-

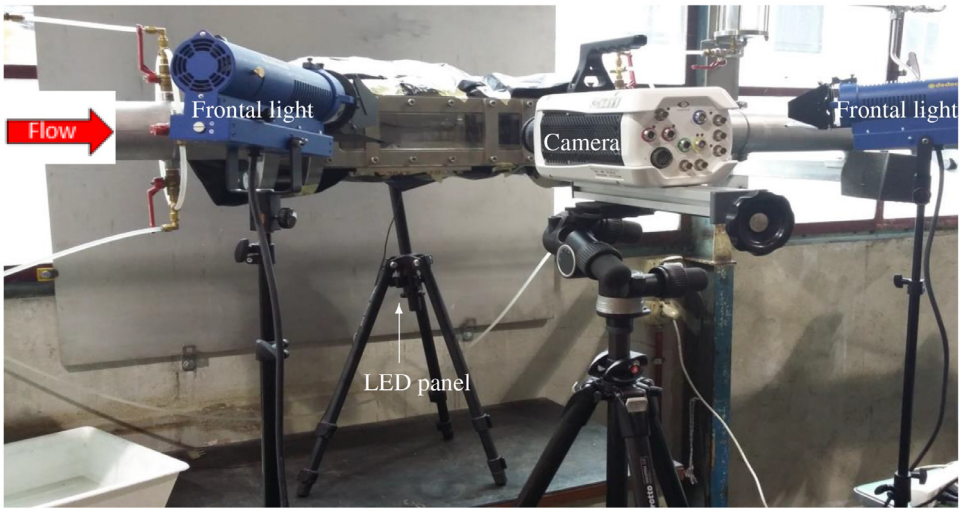

Fig. 2. The basic arrangement and components of the high-speed imaging and the light sources. The bulk flow occurs from the left to right.

tion for liquid volume fraction, where the mass transfer between the phases is defined as an explicit source term to the equation and surface tension effects are assumed small and are neglected. Here, we consider an incompressible flow model, motivated by the balance of computational cost and model accuracy in the current application and turbulence is modelled using Implicit Large Eddy Simulation (ILES) approach.

The LES continuity equation with mass transfer is given by

$$\frac{\partial \bar{u}_i}{\partial x_i} = \left(\frac{1}{\rho_l} - \frac{1}{\rho_v}\right)\dot{m}. \tag{2}$$

The RHS term is the effect of vaporization and condensation, where ρ_l is the liquid density, ρ_v is the vapour density and $\dot{m}$ is the rate of mass transfer between phases and is obtained from a finite mass transfer (FMT) model. Further, the Navier-Stokes equations are

$$\frac{\partial(\rho_m \bar{u}_i)}{\partial t} + \frac{\partial\left(\rho_m \bar{u}_i \bar{u}_j\right)}{\partial x_j} = -\frac{\partial \bar{p}}{\partial x_i} + \frac{\partial}{\partial x_j}\left(\bar{\tau}_{ij} - B_{ij}\right) + \rho_m g_i. \tag{3}$$

In these equations, the overbar denotes low pass filtered quantities, and $B_{ij} = \rho_m(\overline{u_i u_j} - \bar{u}_i \bar{u}_j)$ is the subgrid stress tensor. Here, the implicit LES (ILES) approach is used, where the numerical dissipation is considered enough to mimic the action of B_{ij} (Bensow and Bark, 2010; Drikakis et al., 2009). Also, ρ_m and τ_{ij} are the mixture density and the viscous stress tensor, respectively, which are defined as

$$\rho_m = \alpha\rho_l + (1-\alpha)\rho_v, \tag{4}$$

$$\tau_{ij} = \mu_m\left(\frac{\partial \bar{u}_i}{\partial x_j} + \frac{\partial \bar{u}_j}{\partial x_i} - \frac{2}{3}\frac{\partial \bar{u}_k}{\partial x_k}\delta_{ij}\right), \tag{5}$$

where the pure phase densities are assumed to be constant in the incompressible modelling, and μ_m is the mixture dynamic viscosity, given by

$$\mu_m = \alpha\mu_l + (1-\alpha)\mu_v, \tag{6}$$

and α is the liquid volume fraction which specifies the relative amount of liquid in a given volume, e.g. a computational cell. In this model, the evolution of the volume fraction is calculated by solving a scalar transport equation given as

$$\frac{\partial \alpha}{\partial t} + \frac{\partial(\alpha \bar{u}_i)}{\partial x_i} = \frac{\dot{m}}{\rho_l}. \tag{7}$$

To close the above set of equations, the mass transfer rate, $\dot{m}$, should be specified using an FMT model. There are many numerical models in literature to estimate this term and most of them are based on a simplified form of the well-known Rayleigh–Plesset equation. In this study, the Schnerr–Sauer model (Schnerr and Sauer, 2001) is used, which has been proved in earlier studies to give satisfactory results with reasonable computational cost (Asnaghi et al., 2015; Asnaghi et al., 2018). The vaporization and condensation rates are then given by

$$\begin{aligned}\dot{m}_c &= C_c\alpha(1-\alpha)\frac{3\rho_l\rho_v}{\rho_m R_B}\sqrt{\frac{2}{3\rho_l|\bar{p}-p_{threshold}|}}\max(\bar{p}-p_{threshold},0),\\ \dot{m}_v &= C_v\alpha(1+\alpha_{Nuc}-\alpha)\frac{3\rho_l\rho_v}{\rho_m R_B}\sqrt{\frac{2}{3\rho_l|\bar{p}-p_{threshold}|}}\min(\bar{p}-p_{threshold},0),\end{aligned} \tag{8}$$

where $\dot{m}_c$ and $\dot{m}_v$ are the rates of condensation and vaporization, respectively, and $\dot{m} = \dot{m}_c + \dot{m}_v$. In the above equations, R_B and α_{Nuc} are the generic radius and volume fraction of bubble nuclei in the liquid which are obtained from

$$\alpha_{Nuc} = \frac{\frac{\pi n_0 d_{Nuc}^3}{6}}{1+\frac{\pi n_0 d_{Nuc}^3}{6}}, \tag{9}$$

$$R_B = \sqrt[3]{\frac{3}{4\pi n_0}\frac{1+\alpha_{Nuc}-\alpha}{\alpha}}, \tag{10}$$

where n_0 and d_{Nuc} are user defined parameters corresponding to the number of nuclei per cubic meter and the nucleation site diameter, respectively, and they are assumed to be 10^{10} m^{-3} and 10^{-5} m. Also, C_c and C_v are the condensation and vaporization rate coefficients in OpenFOAM (OpenFoam, 2013) which are set equal to 100 in this study. $p_{threshold}$ is a threshold pressure at which the phase change is assumed to happen, usually considered as the vapour pressure of the fluid, which is 2320 Pa in the current simulations. Finally, the liquid and vapour densities are assumed to be $\rho_l = 998.85$ kgm^{-3} and $\rho_v = 0.02$ kgm^{-3}, and the corresponding dynamic viscosity values are set as $\mu_l = 0.00109$ $kgm^{-1}s^{-1}$ and $\mu_v = 1.39 * 10^{-5}$ $kgm^{-1}s^{-1}$.

To solve the governing equations, the interPhaseChangeFoam solver of OpenFOAM was used, in which the pressure (continuity) and velocity (momentum) equations are coupled using a PIMPLE algorithm. This algorithm is a merge of the SIMPLE (Patankar and Spalding (1983)) and PISO algorithms, where the PISO loop is complemented by an outer iteration loop, see e.g. Barton (1998) for

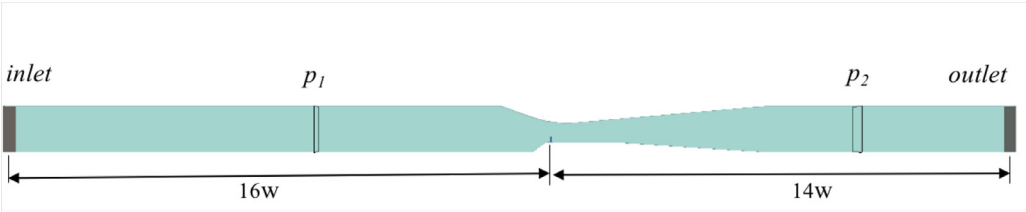

Fig. 3. Computational domain.

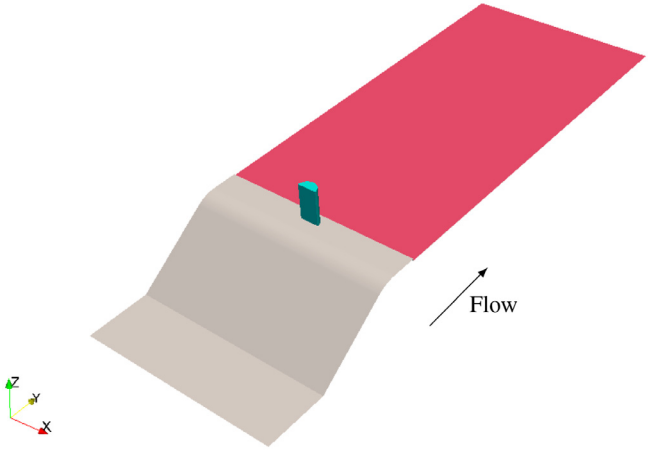

Fig. 4. Lower wall and bluff body.

different ways to merge PISO and SIMPLE procedures. In the current simulations, at each time step, four outer SIMPLE loops are performed, and in each SIMPLE loop, four PISO pressure correction loops are performed. A second order implicit time scheme is used for time discretization and for all simulations the maximum time step is set between 1×10^{-7} s and 5×10^{-7} s which yields a maximum Courant number of $0.3 - 1.5$. The momentum equation convection terms are discretized using a second order central differencing scheme. All of the gradients have been corrected to consider non-orthogonality of the computational cells. For the volume fraction transport equation, a first order upwind scheme is employed and in order to improve the coupling between the volume fraction equation and velocity-pressure equations, the transport equation of the liquid volume fraction is solved inside the PIMPLE loop.

2.5. Numerical geometry and boundary conditions

The created numerical domain is depicted in Fig. 3, including the domain inlet and outlet boundaries as well as the pressure probe locations and the small cylinder in the converging-diverging section of the channel. In order to avoid the influence of the inlet and outlet boundaries on the flow field in the converging-diverging part of the channel and the measured pressure at the probe locations, these boundaries are located far enough from the test section. In the figure, w denotes the channel width normal to the plane, which is constant in the whole domain. At the inlet a constant volume flow rate condition is applied for velocity field while the pressure gradient is set to zero. At the outlet a constant pressure is set such that the probe pressure p_2 is equal to the equivalent experimental value, while zero gradient condition is set for the velocity. Furthermore, a no-slip condition is applied on all solid boundaries including the bluff body. In Fig. 4, the semi-circular cylinder as well as the sloped wall and the behind flat plate are depicted for a more clear understanding of the flow geometry. It

Table 1
Grid study result.

	Number of cells		Predicted values	
	(Total)	(Test section)	$\Delta p(kPa)$	C_D
Main grid	4.8 M	2.5 M	46.5	3.51
Finer grid	10.8 M	6.7 M	47.3	3.57

should be mentioned that it was not possible to measure the turbulence intensity or some other turbulence characteristics at the inlet using the the available equipments in the experiment. Therefore, in the LES simulations inflow turbulence is not taken into account. However, the turbulence inflow to the test section is not expected to have a significant effect on the presented results.

To discretize the flow domain a structured mesh consisting of 4.8 million cells is created using ANSYS/ICEM. The top and side views of the generated grid are shown in Fig. 5 with zoomed views around the body and lower wall. The 0.5 mm height backward facing can be seen in the zoomed views. The mesh is non-uniform with finer cells around the cylinder and near the walls. As will be shown later, different cavity structures are created which may start in front of the cylinder and extend to the end of the flat plate behind the body. If we consider the area from the start of the sloped wall to the end of the flat plate behind the cylinder as the critical area, 2.5 million cells of the generated grid are located in this zone. Also, the length of the cavitating wake in the axial direction is discretized by about 150 grid nodes, while the number of nodes used for the cavity height and width are about 65 and 45, respectively. The first cells on the cylinder and the surrounding walls around it have a height of 0.015 mm which leads to a y^+ value below 7. Usually finer cells should be utilized near the wall boundaries for a proper wall resolved LES, however in this study, the interest is in the separated flow structures that are not influenced by a boundary layer.

To study the influence of grid resolution in the predicted results, however, the flow field was calculated using a finer grid with 10.8 million cells as well. In the finer mesh, the critical area is decomposed by 6.7 million cells and the number of nodes along the cavity length, height and width are about 240, 90 and 60, respectively. In this study, the numerical simulations have been performed for two cavitation numbers, corresponding to experimental case numbers 3 and 6 (Table 2). In Table 1, the obtained results of the two grids for case 6, which has a lower cavitation number and higher Reynolds number, are compared with each other. The predicted values are the pressure drop (Δp) between the two measuring point (Fig. 1) and the drag coefficient on the bluff body. From the predicted values, it was found that using a finer grids does not alter the averaged flow parameters considerably and therefore the 4.8 M cell grid was used in this study.

3. Results

In this section the cavitating flow results for different conditions are presented. This includes cavity profiles and cavitation

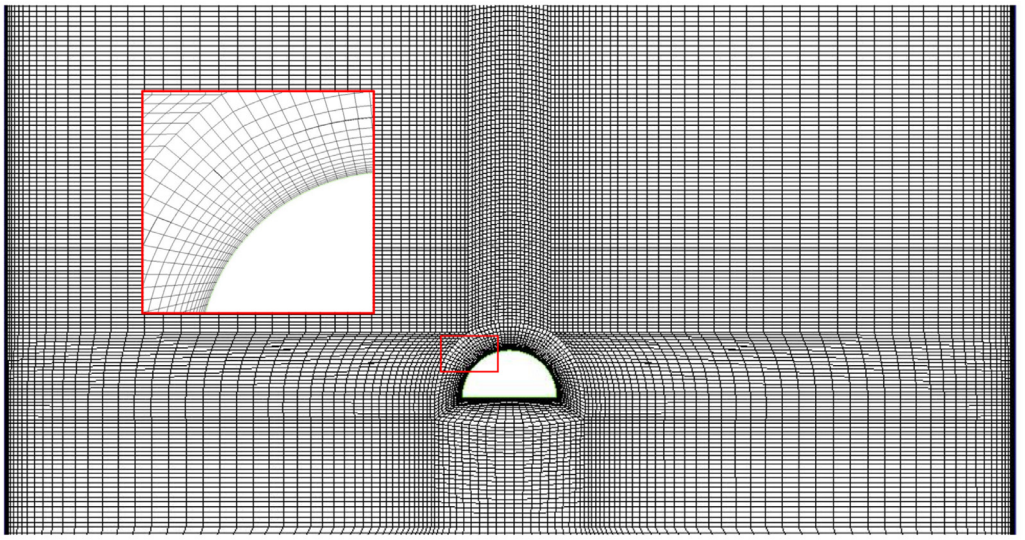

(a)

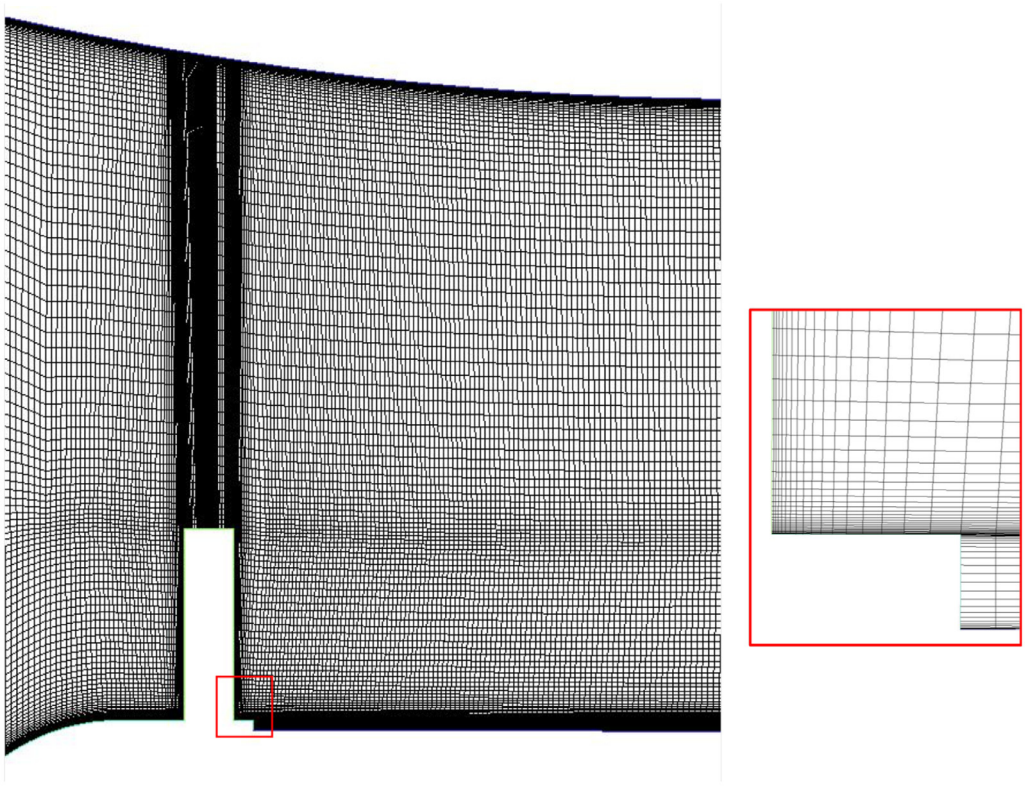

(b)

Fig. 5. Domain discretization: (a) top view; (b) side view.

patterns for different cavitation numbers as well as the cavity effect on the flow behaviour. Details of different test conditions are given in Table 2. In this table, the non-dimensional numbers are based on the average velocity at the channel throat (u_{th}), the average downstream pressure (p_2) and the cylinder diameter (D) as the reference values.

The study has been performed in the cavitation number range of 1.69 to 0.56, however for cases -1 and 0, the flow is almost cavitation free. For case 1, in which the downstream pressure is 1.29 bar, small vapour structures are seen in the domain. Also, as will be shown later, by decreasing the cavitation numbers various cavity patterns are generated in the domain from periodic shedding structures to large supercavities that fully cover the flat surface behind the body at the cavitation number of 0.56. Following Fry (1984), cavitation behind bluff bodies can be categorized into three types: cyclic, transitional and fixed cavitation. A cyclic cavity sheds periodically from the body, while for a fixed type pattern a major portion of the cavity remains attached to the body and small portions may shed from the trailing edge of the attached part. A transitional cavity includes both of these phenomena. In the following sections, the three types of cavity patterns behind the cylinder will be discussed. In Fig. 6, the time-averaged side view

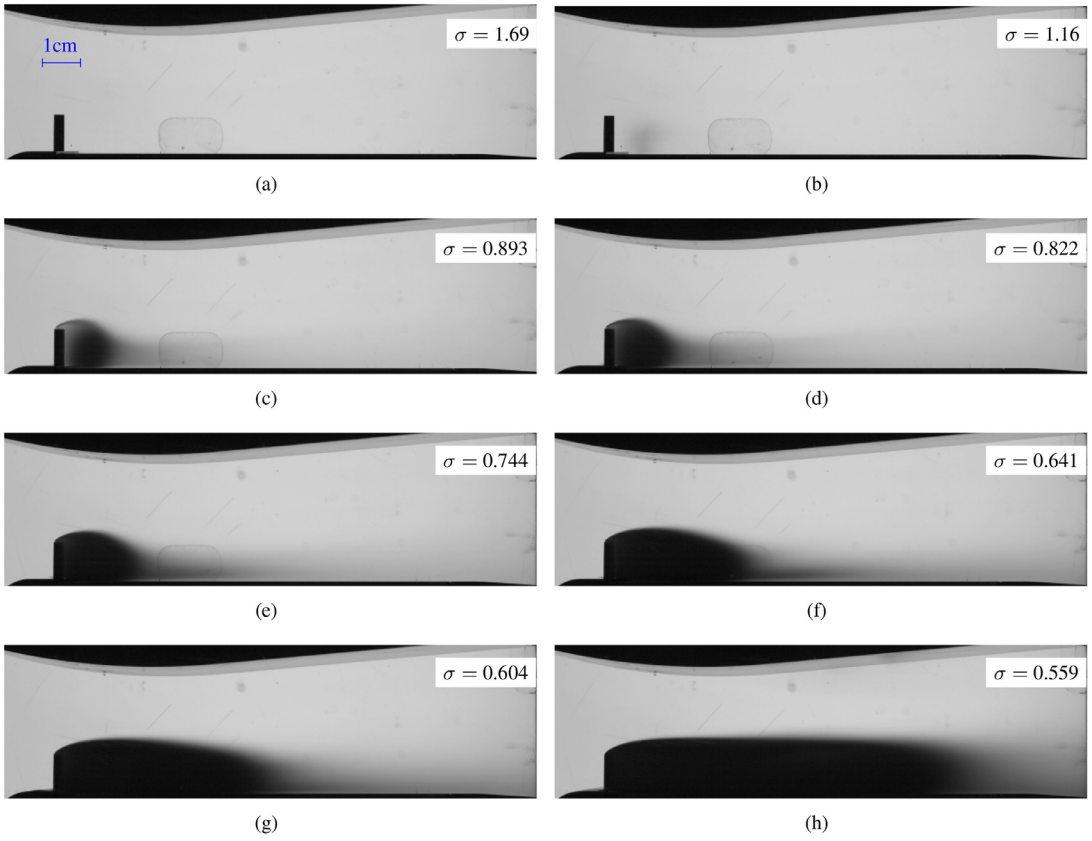

Fig. 6. side view of the time averaged cavities for different cavitation numbers (light condition LC2).

Table 2
Test cases.

No.	p_1(bar)	Q(m^3/s)	Δp(bar)	Re ($\times$ 10^4)	σ
-1	1.122	0.015	0.065	5.6	1.69
0	1.248	0.0175	0.087	6.5	1.37
1	1.403	0.0201	0.114	7.4	1.16
2	1.646	0.0237	0.157	8.7	0.964
3	1.803	0.0257	0.184	9.5	0.893
4	2.0	0.0282	0.219	10.4	0.822
5	2.36	0.032	0.279	11.8	0.744
6	3.36	0.0408	0.441	15.1	0.641
7	4.25	0.0471	0.608	17.4	0.604
8	6.22	0.0582	1.068	21.5	0.559

images of the cavity profiles for different test cases are depicted. It should be emphasized that the flow around the body is confined by channel walls. Although the cylinder frontal area is less than 4 percent of the minimum cross section of the channel, the cylinder height is comparable to the channel minimum height. Therefore, the effects of the bluff body blockage and solid walls are important in the presented results, especially for the fixed cavity pattern.

In Fig. 7, the pressure drop through the test section and average cavity length are shown for different cavitation numbers. In this figure, $K = \frac{p_1 - p_2}{0.5\rho u_{th}^2}$ is the non-dimensional pressure drop in the test section, as measured by the pressure transducers (Fig. 1). For the determination of cavity length, about 6000 images from each case were averaged and a threshold of 20% of the maximum grayscale intensity is selected to obtain the end point of the cavity length. However, for σ = 1.16 and 0.893, as the grayscale intensity was low as compared to the rest of the cases (can be seen in Figs. 6(a) and (b)), the threshold was lowered accordingly. In the pressure loss plot, it is observed that by decreasing the cavitation number

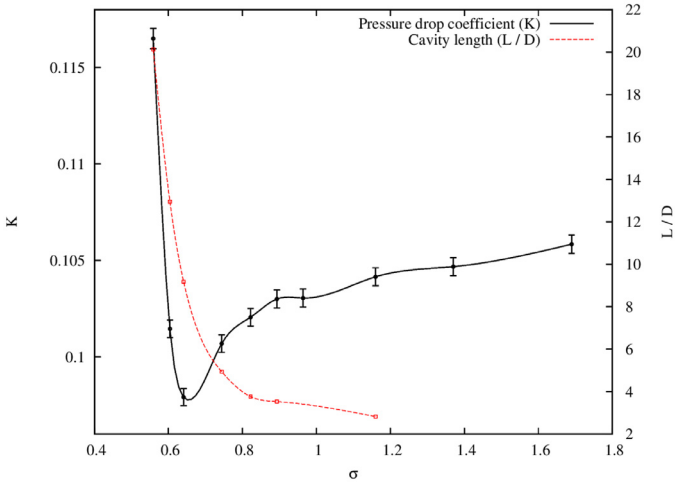

Fig. 7. Non-dimensionalized pressure loss coefficient (K) and average cavity length (L / D) versus cavitation number.

(increasing the Reynolds number) the pressure loss has a slight reduction at first since the boundary layer momentum thickness decreases. Then the plot has a sharp drop with a minimum value at $\sigma = 0.64$, which is due to the lubrication effect of the vapour. In this area the generation and shedding of cavitating vortices reduce the effective fluid viscosity and friction loads on the body. By further decreasing of the cavitation number below $\sigma = 0.64$, the pressure drop increases substantially. For such cases, the cavity structures in the wake area are large enough to considerably narrow the effective channel cross section and the pressure loss over the channel increases.

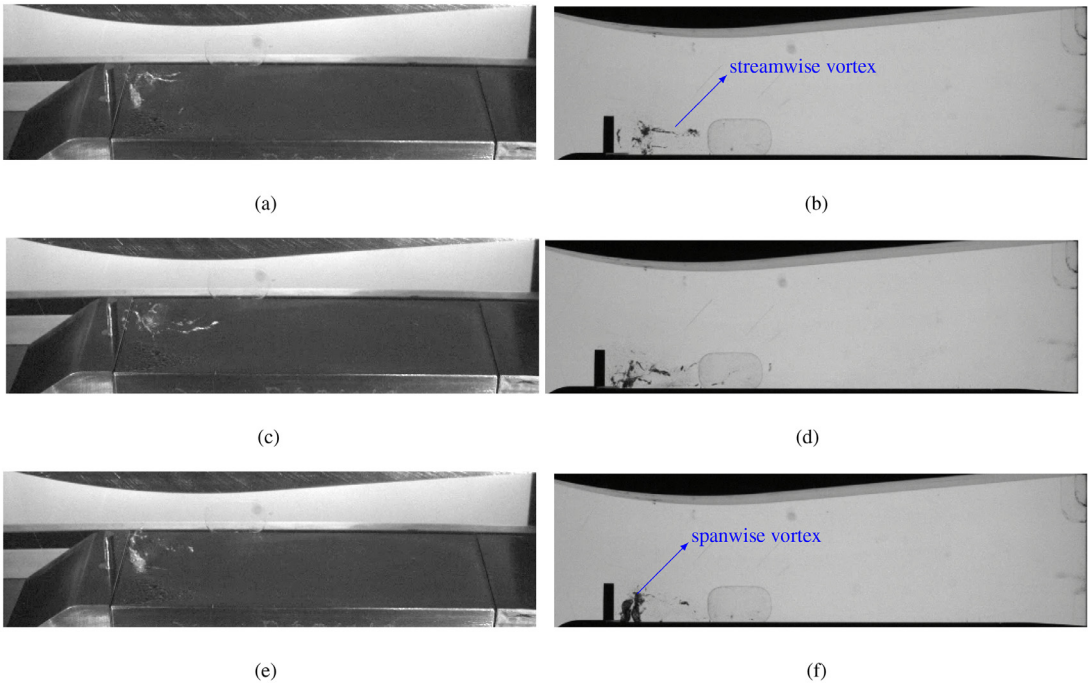

Fig. 8. Cavitation inception at $\sigma = 1.16$; (a), (c), (e): inclined-top view (light condition LC1) (b), (d), (f): side view (light condition LC2).

3.1. Cavitation inception

Cavitation inception occurs when the outlet cavitation number is about $\sigma = 1.16$, Fig. 6(b). Various instantaneous images of this case (case 2 in Table 2) are depicted in Fig. 8 from both the side and the inclined top views; the images are related to different time instances. After separation of the flow from the cylinder edges and in the wake region, different vortices are generated in the stream-wise, spanwise and transverse directions. Here, by streamwise we mean the main flow direction, while spanwise is the direction along the cylinder span and normal to the flat plate behind it and transverse in the other cross-stream direction normal to the spanwise direction. In fact the low pressure vortices are firstly generated in the spanwise and transverse directions, and from their interactions with each other and the main flow, secondary streamwise vortices are created afterwards. From Figs. 8(a) and (b), it is seen that cavitation inception occurs along the streamwise and spanwise vortices. In Figs. 8(c) and (d) also, we see the instances that the cavities are mainly created in the streamwise direction while Figs. 8(e) and (f) show two instances from side and inclined-top views when the spanwise vortices are the main source of cavitation. In the earlier studies of by Ganesh et al. (2018) and Belahadji et al. (1995), it was observed that in the wake of triangular bluff bodies, cavitation inception appears in the form of small filaments. According to Ganesh et al. (2018), inception occurs mainly within the stream-wise secondary (weaker) vortices that are stretched by the primary (stronger) spanwise vortices. They also observed that cavitation occurs along the cores of spanwise vortices but it is not as strong and visible as the streamwise cavities. However, in the current flow field it is observed that the spanwise vortices not only have considerable contribution to cavitation inception, but even they are more cavitating than other vortices as more vapour content are visible in their cores, Figs. 8(e) and 8(f). The major differences between the flow fields with those of the earlier studies will be explained further in the following sections.

3.2. Cyclic cavitation

With further reduction of the cavitation number, the vortex structures get more cavitating. At the outlet cavitation number of $\sigma = 0.893$ (Case 3 in Table 2), the cavities have a cyclic pattern which means that they shed periodically from the cylinder near-wake area. In Figs. 9(a)–(e), a time series of cyclic cavity development is depicted from inclined-top view with light condition LC1. In this case cavities are generated in different vortices in the streamwise, spanwise and transverse directions. The streamwise and spanwise cavities are visible from inclined-top view (Fig. 9), however the less cavitating transverse vortices are more detectable as large dots in the 2D side view in Fig. 10 (e.g. cavities TC1 and TC2). At time T_0 a spanwise cavitating vortex, C31, is created on the cylinder surface. As this vortex detaches from the cylinder, its vapour content increases and the cavity grows ($T_0 + 5\Delta T$). Meanwhile, a second larger spanwise cavity, C32, is seen downstream of C31. While the first cavity is developing behind the cylinder, the second one is shed from the body and its vapour content is decreasing, Figs. 9(c)–(d). Finally, at time $T_0 + 51\Delta T$ the second cavity is detaching in the form of a horseshoe vortex while C31 is completely developed and has a similar shape as of the second cavity in the beginning of the time series (Fig. 9(a)). Horseshoe vortices are not developed from spanwise cavities alone, but a combination of spanwise and transverse cavities which started at the top edge of the cylinder. The horseshoe cavities cannot last long in this case and they often lose most of their vapour contents before reaching the half length of the flat plate, however in specific times the pressure at the core of the vortex is low enough that it may survive until about two-third of the plate length as shown in Fig. 9(f). Sometimes a horseshoe vortex is not developed, but due to the interactions between cross-streamwise vortices with each other and the main flow, a streamwise vortex is created and stretched which leads to streamwise cavities as can be seen in the figure as well. In Figs. 10(a)–(d), another time series of the flow is

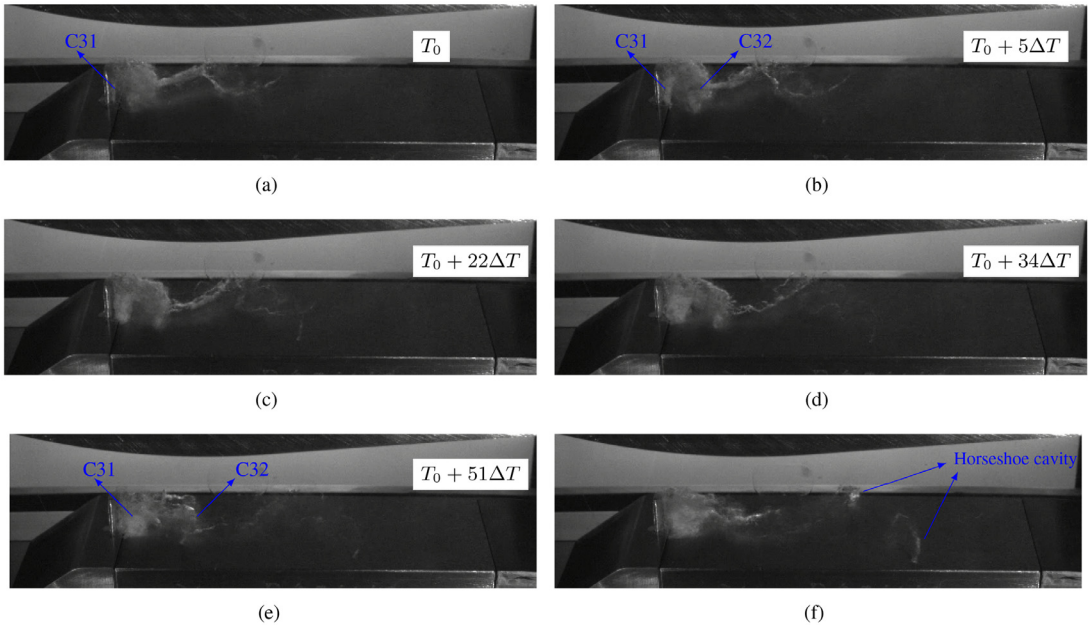

Fig. 9. Instantaneous cavity structures at $\sigma = 0.893$ from inclined-top view (light condition LC1). (a)-(e) represent a time series. For a more clear visualization the reader is referred to video 1, provided as supplementary material to the article.

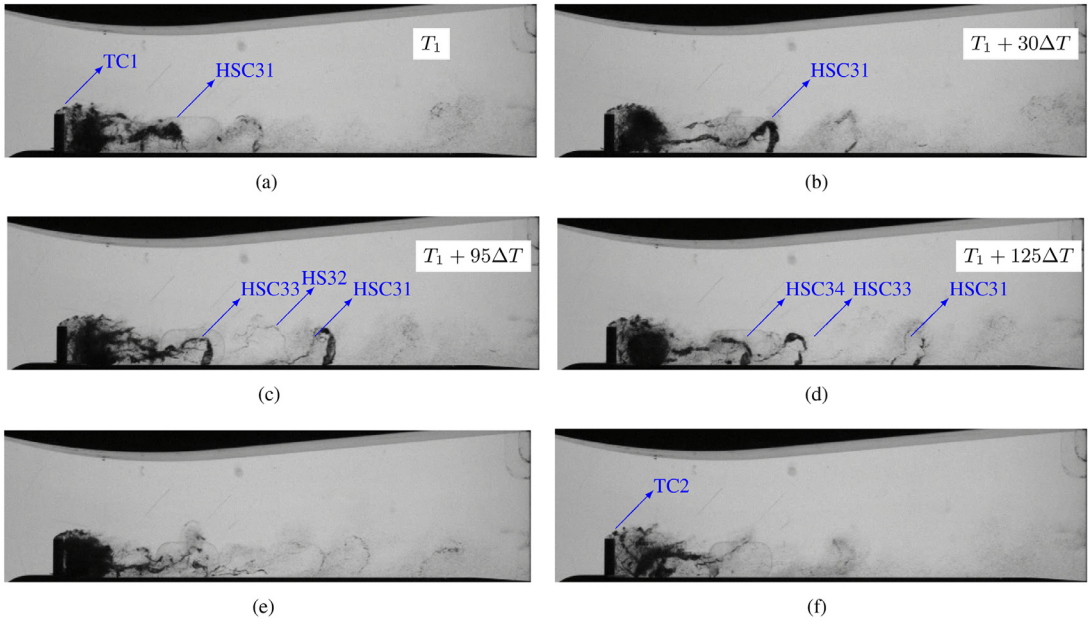

Fig. 10. Instantaneous cavity structures at $\sigma = 0.893$ from side view (light condition LC2). (a)-(d) represent a time series. For a more clear visualization the reader is referred to video 2, provided as supplementary material to the article.

demonstrated from side view with light condition LC2. Fig. 10(a) shows a stretched cavitating streamwise vortex at T_1, and at the end of this structure a horseshoe vortex has started to develop, HSC31; this vortex can be clearly seen at $T_1 + 30\Delta T$. A few time steps later, at $T_1 + 95\Delta T$ and $T_1 + 125\Delta T$, three other horseshoe vortices are shed: HS32, HSC33 and HSC34. While three of the vortices are cavitating, HS32 is almost a non-cavitating, which means that sometimes the pressure at the core of horseshoe vortices does not drop enough to cause vapour generation. The non-cavitating vortex is not as visible as the other structures, however its presence can be further confirmed by the distance between HSC31 and HSC33, which is about twice of the distance between HSC33 and HSC34. Also, in this time series, it is seen that the horseshoe vortices get tilted from their vertical orientation in the side view as they move downstream, and this is due to the axial velocity gradient in the direction normal to the flat plate.

From Figs. 9 and 10, it can also be inferred that the near-wake transverse vortices are less cavitating as compared to their spanwise correspondents. This can be seen from the lower vapour content in the core of the transverse vortices in the side view images. Possible reasons can be the shorter edge of the cylinder in the transverse direction (which leads to smaller vortices) and the flat surface on top side, as compared to the curved semi-circular profile behind the body. It will be shown later that these vortices have less circulation as compared to the spanwise ones. It is also worth mentioning that while at some exceptional instances, dense

cavities with high vapour content can be seen behind the cylinder (e.g. Fig. 10(e)), at most of the other times the near-wake cavities are fully or partially transparent, similar to what is shown in Fig. 10(f).

The described dynamics is different from previous reports on bluff body cavitating flows. As stated, the flow starts to cavitate at the sharp edges of the cylinder, while in the earlier studies of (Ganesh et al. (2018) and Belahadji et al. (1995) for the wedge (triangular prism) test case, cavitating structures were detected in the shear layer and downstream of the body, but not close to the wedge base edge. For a triangular prism, boundary layers are developed on both sides of the body before separation, however, when the flow directly hits a flat front semi-circular cylinder the flow separation at the edge of the body causes more streamline divergence and stronger vortices are created. Also, as the triangular prism has a flat backside, in the nearwake region a dead fluid zone is created which does not happen for the current test case. Moreover, in the mentioned studies, the wedge is confined with solid boundaries on both sides and only streamwise and spanwise cavitating vortices were detected in the wake region, while in the current study the 3D flow passes over the top side of the body which leads to the generation of the transverse and horseshoe vortices.

For further understanding of the flow dynamics, this condition is simulated numerically as well. In Fig. 11, the cavity and vortical structures over a time series of the numerical solution is depicted. In the left column, the cavity structures, represented by an isosurface of liquid volume fraction of 0.99, are seen which are coloured based on their velocity component in the axial direction. Also, the right column of the figure presents the vortices based on the Q-criterion for the relevant time step in the left column. The Q function calculates the second invariant of the velocity gradient tensor and the Q-criterion defines a vortex as a connected fluid region with a positive second invariant of velocity gradient; in other words to represent the vortices we need to plot the regions with $Q > 0$. As there are many vortex structures in the wake region, only higher strength vortices with $Q \geq 10^7$ s^{-2} are depicted in the figure and they are coloured based on the local pressure values. At time T_0, some spanwise cavities exist in the wake area, including a pair of very small cavities just behind the cylinder, a large developed cavity downstream near the shedding location and another middle-size cavity in between. At a later time, a shedding starts from the large downstream cavities while the upstream structures develop further, $(T_0 + 15\Delta T)$. At time $T_0 + 38\Delta T$, we see a horseshoe cavitating vortex, C33, which is formed due to the interaction of spanwise and transverse vortices. When a spanwise vortex is merged with a transverse one, they form a horseshoe vortex which has two legs, an inner leg which is closer to the wake centerline and an outer leg which is closer to the wake boundary and shear layer. Due to the velocity gradient over the width of the wake, the horseshoe vortex is stretched and its core pressure is reduced (it may also be stretched in the wall-normal direction due to the velocity gradient in the wall boundary layer, as explained earlier). Sometimes there is a possibility for the horseshoe vortex to get developed and cavitates like the cavity C33 and sometimes the inner leg is stretched such that the horseshoe vortex is not formed and we only have a streamwise cavity such as C34 at time $T_0 + 88\Delta T$. Considering cavity C34 in Figs. 11(g)–(j) and the lower pressure in the core of the vortex, a mechanism of cavity generation in the wake region is the vortex stretching. According to Chang et al. (2012), the stretching and turning of a secondary vortex by the stronger primary vortex can result in a sharp decrease in the core pressure of the vortex through a reduction in the core size. Also, it is seen that among the large number of vortical structures in the wake region, only a few of the larger vortices are cavitating. Larger vortices have higher circulations and their pressure drop is larger as compared to the smaller vortices in the same area.

The last row of Fig. 11 shows a different instance of the numerical results in which the vapour fraction is higher and larger cavities are developed behind the cylinder. Comparing vortical structures at this time with the earlier instances shows that cavity generation significantly reduces the flow vorticity in the wake area. This is in agreement with what is found in earlier studies. Gnanaskandan and Mahesh (2016), for example, have found that by reducing the cavitation number, fewer vortices are shed over a given distance in the wake of a circular cylinder. They also showed that this reduction in the shedding frequency is due to the dilatation of vorticity in the presence of vapour. In addition, two other minor features can be detected from Fig. 11. The first one is the ring-shaped vortices that are formed in front of the cylinder base (right column of the figure). The other feature is the local pressure increase after the collapse of a cavity which is clearly seen by the red zone in Fig. 10(j). These characteristics are more important in the following cases and will be discussed later.

It should also be mentioned that the average numerical cavity length is about 1.8 cm which is similar to the experimental value (1.76 cm); however, the predicted pressure drop along the test rig $(p_1 - p_2)$ is about 13 kPa, which is considerably different from the experimental value (18.5 kPa, Table 2); this can be related to a general limitation of homogeneous mixture models. In fact, while the vortex cavity generation, its roll-up and shedding in the near wake area are well-represented by the simulations, the collapse rate of the shed vortices is higher than what is seen in the experimental tests. Most of the horse-shoe and streamwise vortices lose their vapour content quickly after shedding. In the homogeneous mixture models the cavitation criterion is simply based on the difference between the local pressure and the vapour pressure, and therefore cavity inception and collapse occurs when the local pressure is below or above the vapour pressure, respectively. However, in reality there are other effective factors (e.g. non-condensible gases) that are neglected in the numerical modelling. These numerical issues are discussed in the earlier study by Gnanaskandan and Mahesh (2016) as well. Besides that, the linear relations in Eq. (8) does not sufficiently represent the inertia of fast collapsing small-scale cavities. Faster collapses can lead to less cavity structures on average, which affects the average pressure drop along the test rig. Such a limitation can be addressed by Lagrangian models in which the small scale cavities and bubble dynamics are represented more appropriately, during both the inception and collapse phase. This is a topic for future study.

3.3. Transitional cavity pattern

By reducing the cavitation number to the lower value of 0.822 (case 4 in Table 2), the cavitation pattern is still cyclic and no considerable difference was found as compared to the depicted results above. With further reduction of the cavitation number to $\sigma = 0.744$ (Case 5 in Table 2), the cavities have a transitional pattern which means that a portion of the cavity remains attached to the body, while large vapour structures are periodically shed from its downstream end. The time-averaged side view image of this case is shown in Fig. 6(e). In Fig. 12, a special time instance of this case is shown, in which a large spanwise cavity, C51, is being developed while a second larger cavity, C52, is about to shed from the attached portion. Here, the near-wake cavities have higher vapour fractions as compared to the previous case. In fact the spanwise vortices seem to be full of vapour. However, the transverse cavities are still less cavitating as compared to spanwise structures. As stated earlier, due to the velocity difference of the inner and outer legs of a horseshoe vortex, the inner leg is sometimes stretched and turns into a streamwise vortex. In Fig. 12, it can also be seen that these vortices can get highly stretched over the flat plate (cavity C53) and sometimes their vorticity is so high and they re-

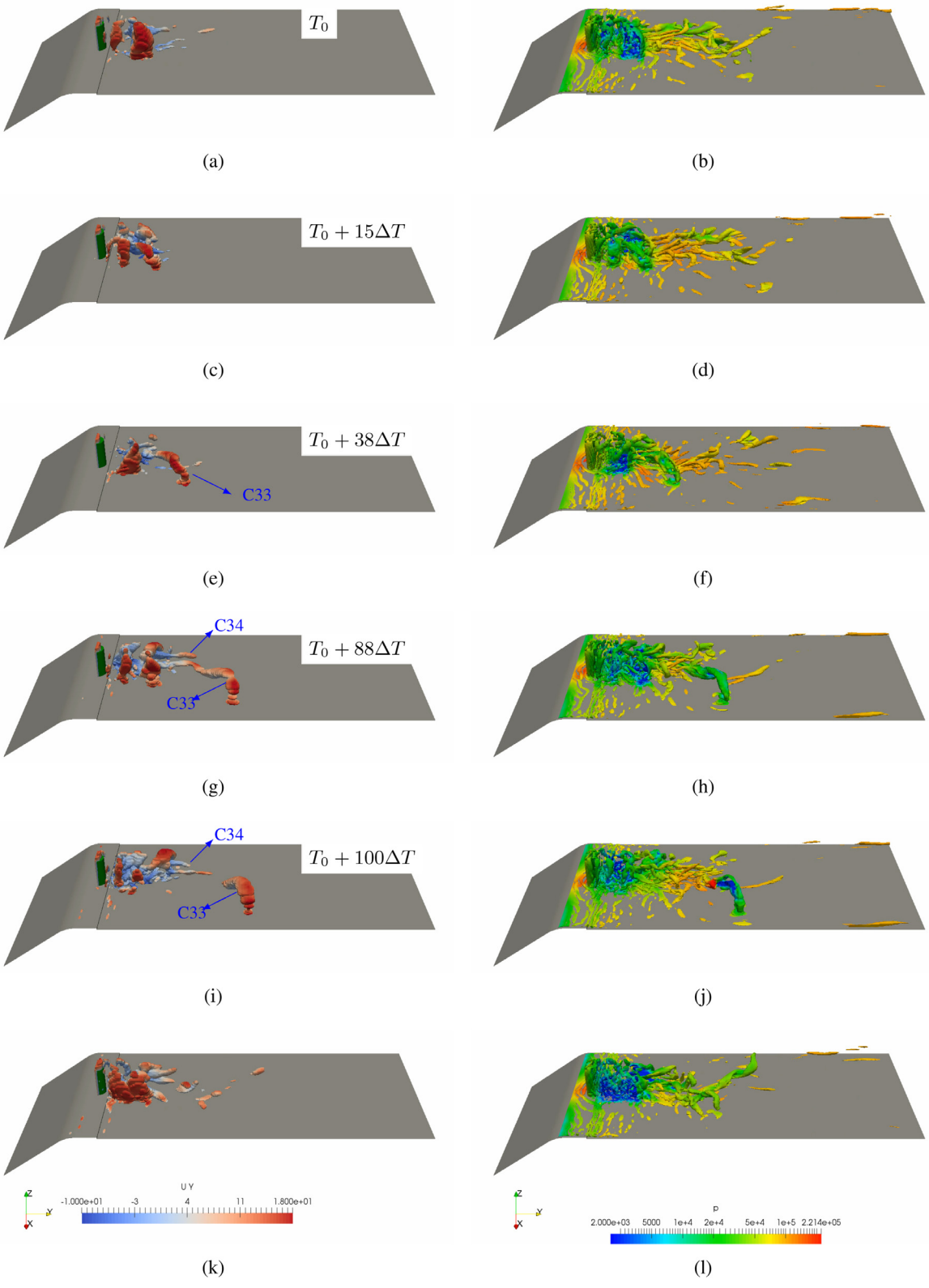

Fig. 11. Instantaneous numerical results for $\sigma = 0.893$. (a), (c), (e), (g), (i), (k): vapour structures with $\alpha = 0.99$; (b), (d), (f), (h), (j), (l): vortical structures with $Q = 10^{7}$ s^{-2}.

main as cavitating for larger distances (cavity C54). However, as mentioned earlier, the cavity structures do not have a regular behaviour, although the general pattern can be considered as repetitive. In fact, sometimes a horseshoe cavity can survive until about 80 % of the flat plate length, such as the structures marked as HSC in Fig. 13(a), while in other instances, its inner leg is stretched such that a horseshoe cavity is not formed at all (e.g. Fig. 12). Another important characteristics of these structures is their relative rate of shedding to the vortex shed on the opposite side of the cylinder. Usually in the wake of bluff bodies, the vortices are shed one-by-

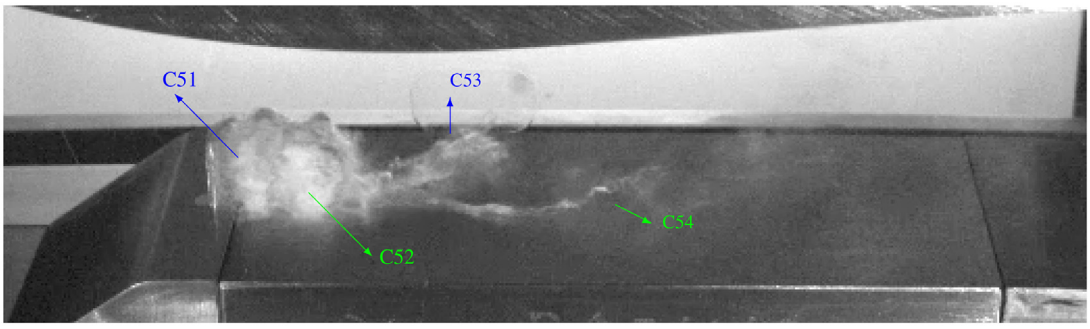

Fig. 12. Different cavity structures at $\sigma = 0.744$; inclined-top view with light condition LC1.

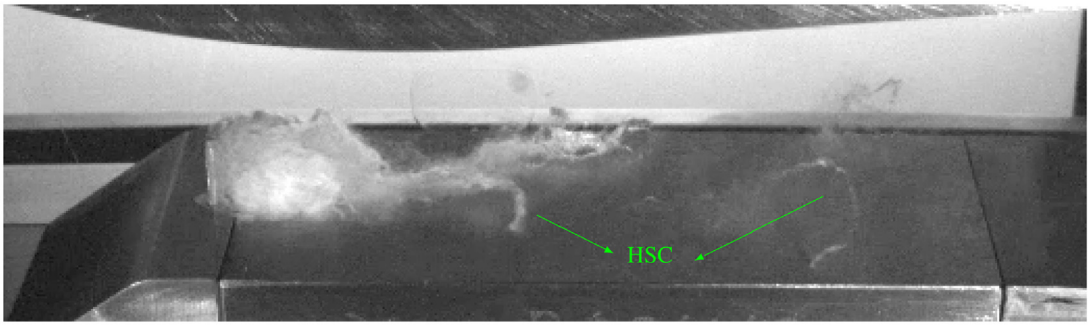

(a)

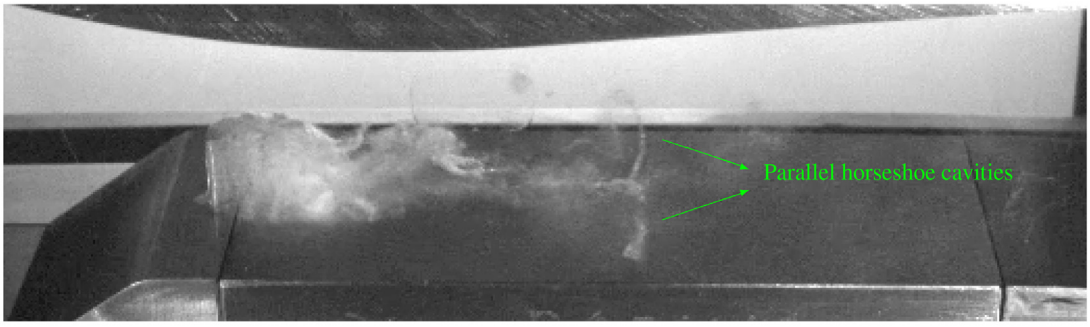

(b)

Fig. 13. Instantaneous images of horseshoe cavities at $\sigma = 0.744$; inclined-top view with light condition LC1.

one from opposite sides of the body; however, in Fig. 13(b), two horseshoe cavities are moving in parallel on both sides of the plate and it can be inferred that their original spanwise vorticities had shed simultaneously (and not one-by-one) from the near-wake region. In other words, sometimes there is no longitudinal distance between spanwise cavities in the wake region. This behaviour is more important in the dynamics of the fixed cavities as will be explained later.

As stated in the numerical results of the previous case, when a cavity structure is collapsing, it emits a pressure wave that affect the neighboring structures. When the flow rate is increased, the vortex shedding and deformation process occurs at a higher rate, which means that the cavity structures have faster collapses in similar situation and it can lead to higher emitted collapse pressures. In Fig. 14, a time series of this test case is depicted in which a streamwise vortex cavity partially collapses at $T_0 + 11\Delta T$. During this collapse, an emitted pressure wave causes subsequent partial collapse of the attached upstream cavity. In Figs. 14(c) and (d), two later instances are depicted in which the streamwise cavity is collapsing while the vapour content of the fixed cavity is decreasing due to a pressure wave that is moving upstream. For a more clear understanding, it is suggested to look at video 3, which is provided as supplementary material to the article.

Finally, in Fig. 15, another instance of the flow is depicted from side view to further demonstrate the cavity patterns and their difference with the earlier case (Figs. 10(a)–(f)). The considerably higher vapour content in the near-wake region is observed in this figure, as well as the more cavitating shed structures. After collapsing, the horseshoe cavities turn into sparse clouds of bubbles which move upward due to the lift force from the main flow.

3.4. Fixed cavity pattern

By reducing the cavitation number to $\sigma = 0.64$ or lower, we reach fixed cavity patterns in which a major portion of the cavity remains attached to the body and small portions shed from the trailing edge of the attached part. The last three cases of Table 2 ($\sigma = 0.641, 0.604, 0.559$) belong to this category and a difference among these cases is the length of the fixed part which varies considerably with a small change in the cavitation num-

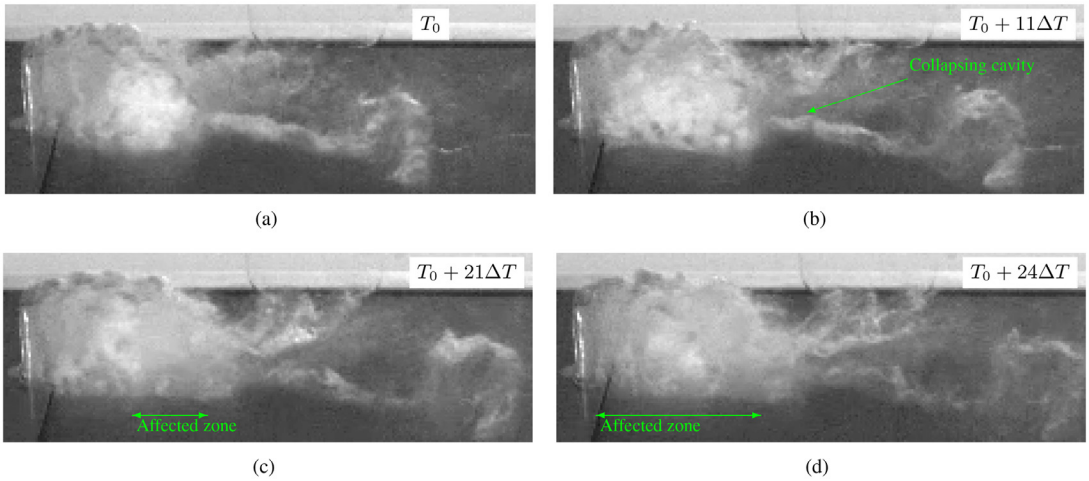

Fig. 14. A time series of partial cavity collapse at $\sigma = 0.744$; inclined-top view with light condition LC1. For a more clear visualization the reader is referred to video 3, provided as supplementary material to the article.

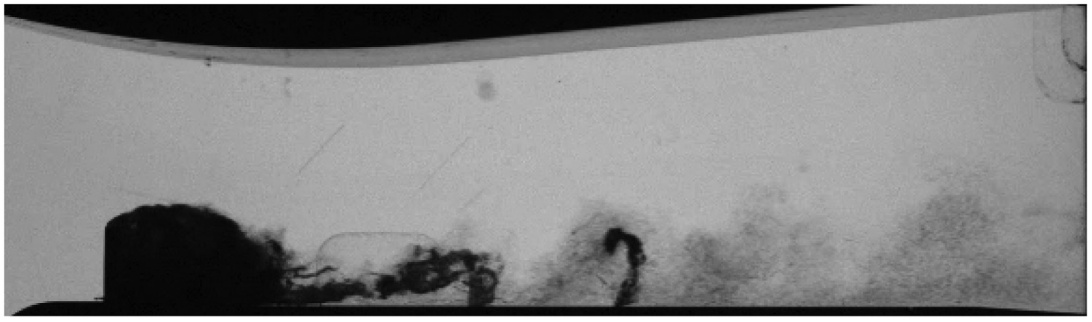

Fig. 15. An instantaneous side view of the case ($\sigma = 0.744$) (light condition LC2).

ber, as shown by time-averaged images in Figs. 6(f)–(h). In Fig. 16, two time instances of the cavity structures of cases 6 and 8 from inclined-top view are shown to demonstrate some features of the flow. In addition to the shedding of smaller structures at the end, the dynamics and shape of fixed portion have considerable variations with time. Sometimes this part has a smooth interface with the surrounding liquid (e.g. 16(a)), while at another time this surface can be quite disturbed (e.g. 16(b)). Also, sometimes the fixed cavity gets completely detached from the cylinder and moves downstream, while at the same time a new fixed cavity starts to develop from the body edges and a temporary ring-shaped vortex cavity is generated in front of the cylinder base. Such phenomena are observed in Fig. 16(b), where the dashed line shows the upstream end of a detached cavity.

By investigating the flow field, it is found that the large cavity detachment from the body occurs when a reverse flow of vapour inside the fixed portion moves upstream and hits the cylinder backside. This process is demonstrated by a special time series for $\sigma = 0.604$ in Fig. 17. The reverse flow occurs inside the fixed cavity and it can be distinguished by the variation in the image intensity. In the left column of the images, the unprocessed snapshots of this time series is depicted in which the intensity of the fixed cavity portion is increasing from its trailing to the leading edge over the series. The forefront edge of the reverse flow is also marked in the figure by a dashed line. In order to improve the contrast, an image adjustment operation is performed on the high-speed images for this case. This process involves rescaling the grayscale intensities in order to have 1% of the data being saturated at high intensities and 1% of the data covering low intensities. With this operation, the values of the grayscale intensities then vary between 0 and 255, as shown in the right column of Fig. 17. In each row of the figure, the processed right side image corresponds to the same time instance as of the left side snapshot. It should be noticed that the processed images are created based on the intensity of the whole image and therefore, the white and red zones around the cavity are due to the white background of the image. As the front edge of the reverse flow moves upstream, we can see larger red and white zones in the cavity which is an indication of increased intensity. The reverse flow phenomenon will be further verified with numerical results later.

As the reverse vapour flow moves upwards, due to its interaction with the main flow the cavity interface gets disturbed and it can be observed in the left column of Fig. 17, where in each instance the upstream part of the interface (left side of the dashed line) looks smooth while the downstream part is disturbed. At time $T_0 + 185\Delta T$, the reverse flow hits the cylinder and the whole interface has already got disturbed. After the strike, the whole cavity is detached from the cylinder and a new attached cavity starts to develop from the edges of the cylinder ($T_0 + 225\Delta T$). This series of phenomena occurs repeatedly in the flow field, however in a nonperiodic pattern. In fact, sometimes the reverse flow does not reach the end of its path and the detachment occurs in the middle of the fixed cavity. Also it happens quite frequently that a second reverse flow starts from the end of the fixed cavity while an earlier disturbance has not reached the cylinder yet and it is not easy to distinguish separate reverse flow from each other. In fact, the time series of Fig. 17 is one of the exceptional time periods that includes a rather clear isolated reverse flow. Besides that, the detachment-redevelopment process of the fixed cavity occurs so fast that sometimes it is difficult to distinguish the new and old attached cavities

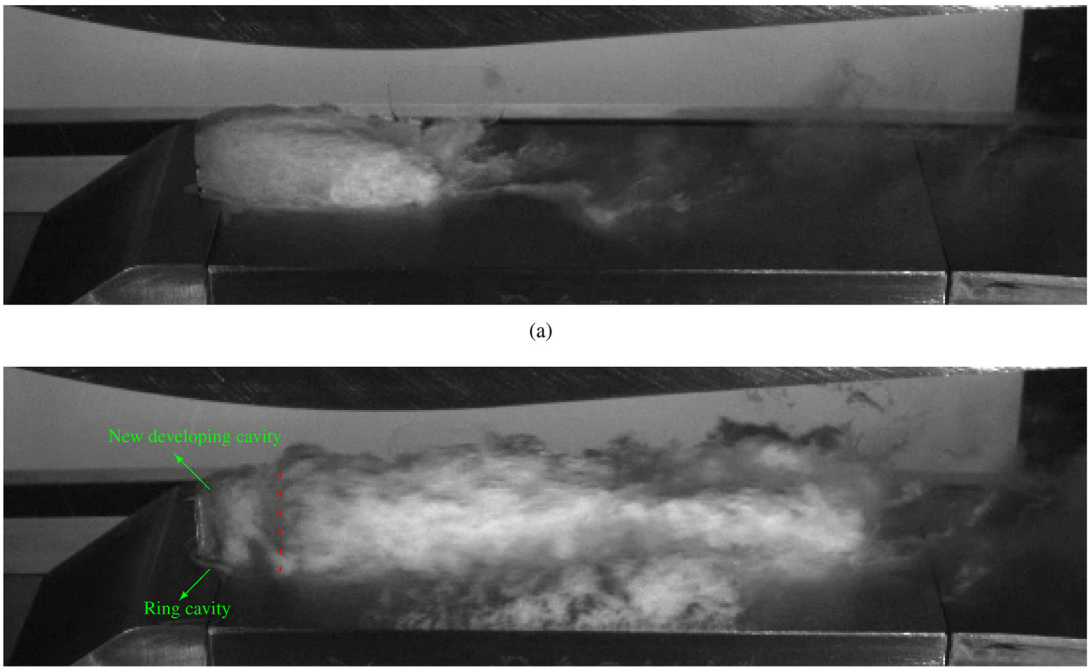

(a)

(b)

Fig. 16. Two times instances of fixed cavity patterns: (a) $\sigma = 0.641$; (b) $\sigma = 0.559$; the red dashed line locates the upstream end of the detached cavity. (For interpretation of the references to colour in this figure legend, the reader is referred to the web version of this article.)

from each other using video snapshots. While in Fig. 17(m), this phenomenon is less visible, Fig. 16(b) gives a more clear picture of such a moment.

Also, a ring-shaped vortex cavity is generated when the reverse flow hits the cylinder and the fixed cavity detaches, which is not visible in the side view images of Fig. 17, but it can be observed in Fig. 16(b). As will be shown in the numerical results, some ring-shaped vortices always exist in front of the cylinder base, and their core pressure is high enough that they do not cavitate. However, when a reverse flow moves toward the cylinder, it changes the pressure field around the body and it seems that the closest vortex is stretched and cavitates temporarily.

The exact physical reason for the reverse vapour flow is not completely clear, however, it seems that this flow occurs after a violent collapse or shedding of cavities at the trailing edge of the fixed portion. In Fig. 18, a few earlier time steps before time T_0 (Fig. 17(a)) are depicted. At time $T_0 - 170\Delta T$, a cavity structure is detached at the end of the profile, which can be due to interaction of vortices from different alignments. After this shedding, another vapour structure gets detached from the fixed portion, but at a more upstream location ($T_0 - 120\Delta T$ to $T_0 - 110\Delta T$). Fig. 18(d) shows the moment that the second cavity is detached from the body. At a later time step ($T_0 - 70\Delta T$), a third and larger cavity is detached at a further upstream point (almost at the middle of the fixed cavity). After the full detachment of this structure, the main reverse vapour flow starts from the closure line of the fixed cavity. Time $T_0 - 50\Delta T$ is 2 msec earlier than T_0 in Fig. 17(a). When a cloud cavity detaches from the fixed portion, it starts to collapse and a pressure wave is emitted from the collapse starting point which leads to subsequent collapse of other parts of the cloud. This can be seen by the lower cavity content of the detached clouds at times $T_0 - 110\Delta T$ and $T_0 - 50\Delta T$. The emitted pressure wave is also seen in the transitional cavity pattern, as explained earlier. Although this pressure wave can temporarily increase the local pressure around the collapse point, it does not seem to be strong enough to cause a continuous force which can drive the reverse flow for a longer period of time. It seems most likely that the main reason for reverse vapour flow is the interaction of various vortices, including spanwise vortices with opposite circulations from both sides of the cylinder and the transverse vortices. The vortex interactions (collisions) can increase the local flow pressure, especially when they are in opposite directions. As it was shown for the transitional cavity pattern as well, it is possible for the cavitating flow around a semi-circular cylinder that two spanwise cavities with opposite circulations move parallel and meet at the end of the near-wake area (before detachment). Particularly, if the parallel shed vortices are fixed at the end of the cavity (even for a short period), they can feed the upstream flow in the center. Another possible explanation for the reverse flow can be the pressure fluctuations during the shedding process. It is known that in single phase flow around a bluff body, due to the detachment and shedding of vortices, the pressure field around the body fluctuates, which leads to the time variation of the drag force on the body. In this cavitating flow, however, the detachment point is moved to a further downstream point and the vortices shed at the end of the fixed cavity. Therefore, the pressure varies periodically, and a fluctuating force (similar to the bluff body drag force) is exerted on the fixed cavity at its end, and this force (or pressure variation) causes repeated reverse flow of vapour.

Regardless of the main source of the reverse flow, the cavitation pattern follows the general behaviour of a supercavity. According to Franc and Michel (2006), at a supercavity closure two main regimes occur and alternate with each other: a re-entrant jet (similar to the current reverse vapour flow) that tends to confine the gas and vapour inside the cavity; and an emission of limited coherent trains of alternate vortices (similar to the current shedding of small cavities). Supercavity flows around different bodies have been modelled in literature using steady potential flow theory and some closure models have also been proposed to explain the complex phenomenon at the closure (Franc and Michel, 2006). For example, Tulin model (Tulin, 1963) assumes that cavity is terminated by two spiral vortices resulting from superimposing conditions on

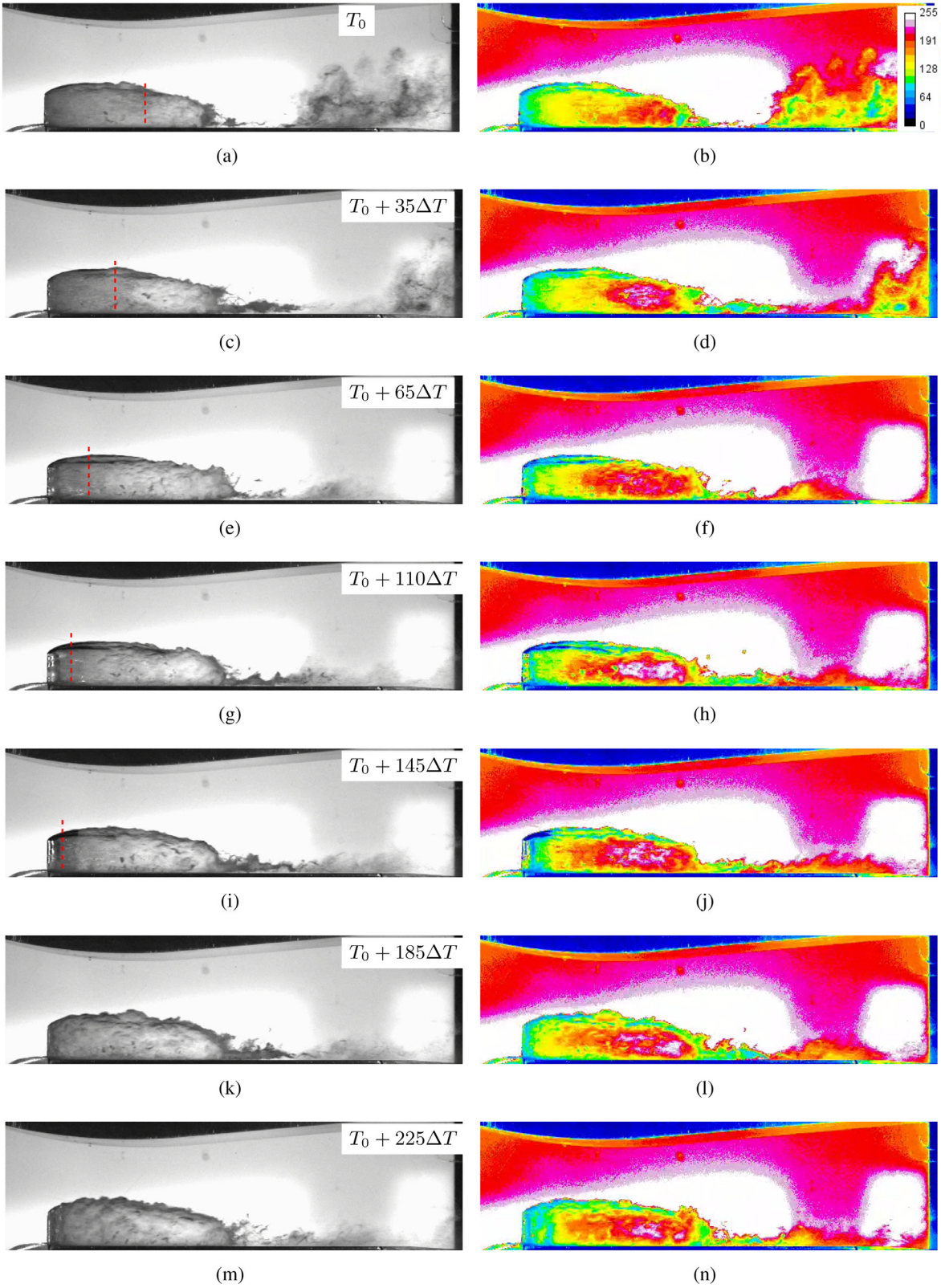

Fig. 17. A time series of instantaneous images at $\sigma = 0.604$. The dashed line locates the frontal edge of the upstream moving disturbance. (a), (c), (e), (g), (i), (k), (m): grayscale images with light condition LC1; (b), (d), (f), (h), (j), (l), (n): processed images. For a more clear visualization the reader is referred to videos 4 and 5, provided as supplementary materials to the article.

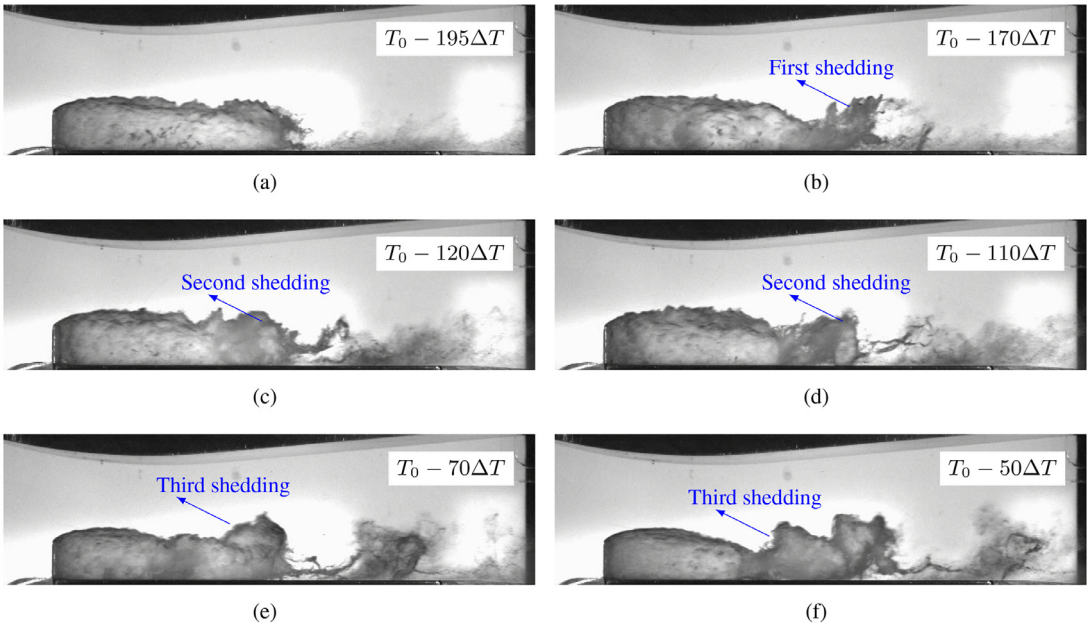

Fig. 18. A time series of instantaneous images at $\sigma = 0.604$; A few time steps before the reverse vapour flow of Fig. 17. side view with light condition LC1. For a more clear visualization the reader is referred to video 6, provided as supplementary material to the article.

the cavity and its wake. However, as in the current problem, we have a 3D unsteady flow that is confinded by channel walls and there is a flat surface below the supercavity, the potential flow theory cannot be applied here. It should also be emphasized that the blockage effect is an important parameter in a flow confined with solid walls. In such a flow, the cavity length can become finite if the cavitation number gets lower than a critical value.

For further understanding of the flow dynamics, one of the test cases of this category is simulated numerically as well. In an earlier study, Ghahramani et al. (2019) showed that for the FMT based homogeneous mixture models, using larger empirical constants (C_c and C_v is Eq. 8) leads to more satisfactory results. By increasing the flow Reynolds number and decreasing the cavitation number, the flow field gets numerically more unstable and we are limited in using smaller time steps and empirical constants. Therefore, for numerical simulation, case 6 ($\sigma = 0.641$) was chosen for which we can use larger empirical constants with no severe stability issues.

In Figs. 19 and 20, a time series of the numerical solution is depicted. Fig. 19 includes the cavity structure reproduced by an iso-surface of liquid volume fraction of 0.9 that is coloured based on the local axial velocity component in the left column and the liquid volume fraction contour over a 2D plane in the right column; the 2D plane is parallel to the bottom flat wall and cuts the cylinder through its mid-height, y = 0.5 H. Also, the axial velocity contour over the same plane is plotted in the left column of Fig. 20, while a top view of 3D vortices is depicted in the right column using Q-criterion with $Q = 10^6$ s^{-2}. The vortices are coloured based on the local pressure. From the 3D plot of cavity structures, it is seen that the axial velocity of the liquid-vapour interface is always positive, however, at time T_0 we can see negative velocity at the tail of the fixed cavity which is an indication of a reverse flow. This phenomenon can be detected more conveniently from the velocity contours. It should be mentioned that the global range of the axial velocity is larger than the plot legend, however, the legend range is limited to increase the image contrast. As the blue zones show the negative velocity areas, it can be inferred from the 2D velocity contours that, even before the time T_0, the velocity inside the fixed cavity area is negative. It seems that the liquid-vapour interface is a shear layer and the vapour behind it usually moves in the reverse upstream direction. In fact, what we see from the experiment is not only a reverse flow, but a disturbance with a higher momentum than the initial reverse flow of vapour, which increases the absolute value of this negative velocity. At time $T_0 + 75\Delta T$, the high momentum flow has passed about 3/4 of its way towards the cylinder, as can be seen from the velocity contour. Comparing the cavity structures and 2D vapour fraction contours between times T_0 and $T_0 + 75\Delta T$ shows how this flow disturbs the liquid-vapour interface, not only in the shape but also vapour fraction value at this boundary. At time $T_0 + 100\Delta T$, the reverse flow hits the back side of the cylinder and the fixed cavity is about to detach from the body (more visible in Figs. 19(f) and 20(e)). This flow also increases the vorticity in the vapour zone, as can be seen by comparing the vortical structures in the first three time steps. Also, the variation in the vapour fraction field is noticeable. As the flow moves upstream, the vapour volume fraction behind it is decreased, however it does not have the same effect as condensing fronts that are reported in earlier studies (e.g. Gnanaskandan and Mahesh (2016)). Here we do not have a full condensation, and if some parts of the vapour condenses completely (such as the small red zones inside the vapour area in Figs. 19(d) and 19(f)), it will quickly cavitate again. At time $T_0 + 120\Delta T$, the fixed cavity detaches from the body. The detachment of the cavity is more visible at the later time of $T_0 + 150\Delta T$. A comparison between this time and time T_0 shows the significant effect of this accelerating flow and the cavity detachment on the velocity distribution in the wake area as well as the interface shape. At this time, we can also see a new high momentum flow at the tail of the fixed cavity in the velocity contour (Fig. 20(i)). At times $T_0 + 190\Delta T$ and $T_0 + 230\Delta T$ a cavity is shed from the end of the fixed portion on the right side, while the second high velocity flow is moving upstream. Fig. 19(n) demonstrates the unsymmetry in the vapour fraction field and the effect of the vapour shedding on the left side of the fixed cavity during this time. The cavity is shed in the form of a horseshoe vortex at $T_0 + 270\Delta T$, and at the same time the second high momentum flow reaches the cylinder but its impact on the cylinder is less than the earlier disturbance as its kinetic energy is partially dispersed. A comparison between the vortical structures shows that the cavity flow after its detachment from the cylinder further increases the

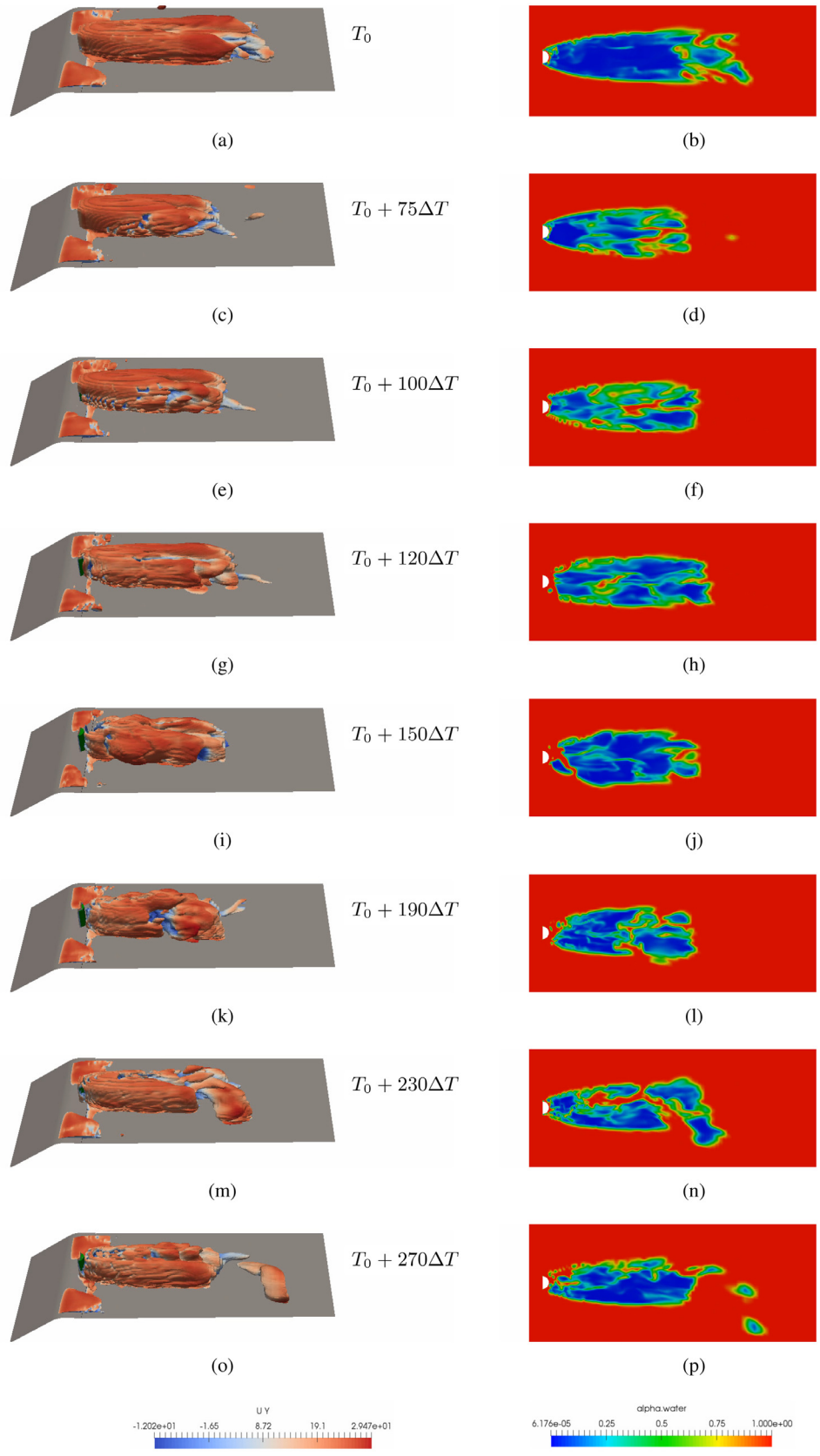

Fig. 19. Instantaneous numerical results for $\sigma = 0.641$. (a), (c), (e), (g), (i), (k), (m), (o): vapour structures with $\alpha = 0.9$, coloured by axial velocity; (b), (d), (f), (h), (j), (l), (n), (p): 2D cavity contours.

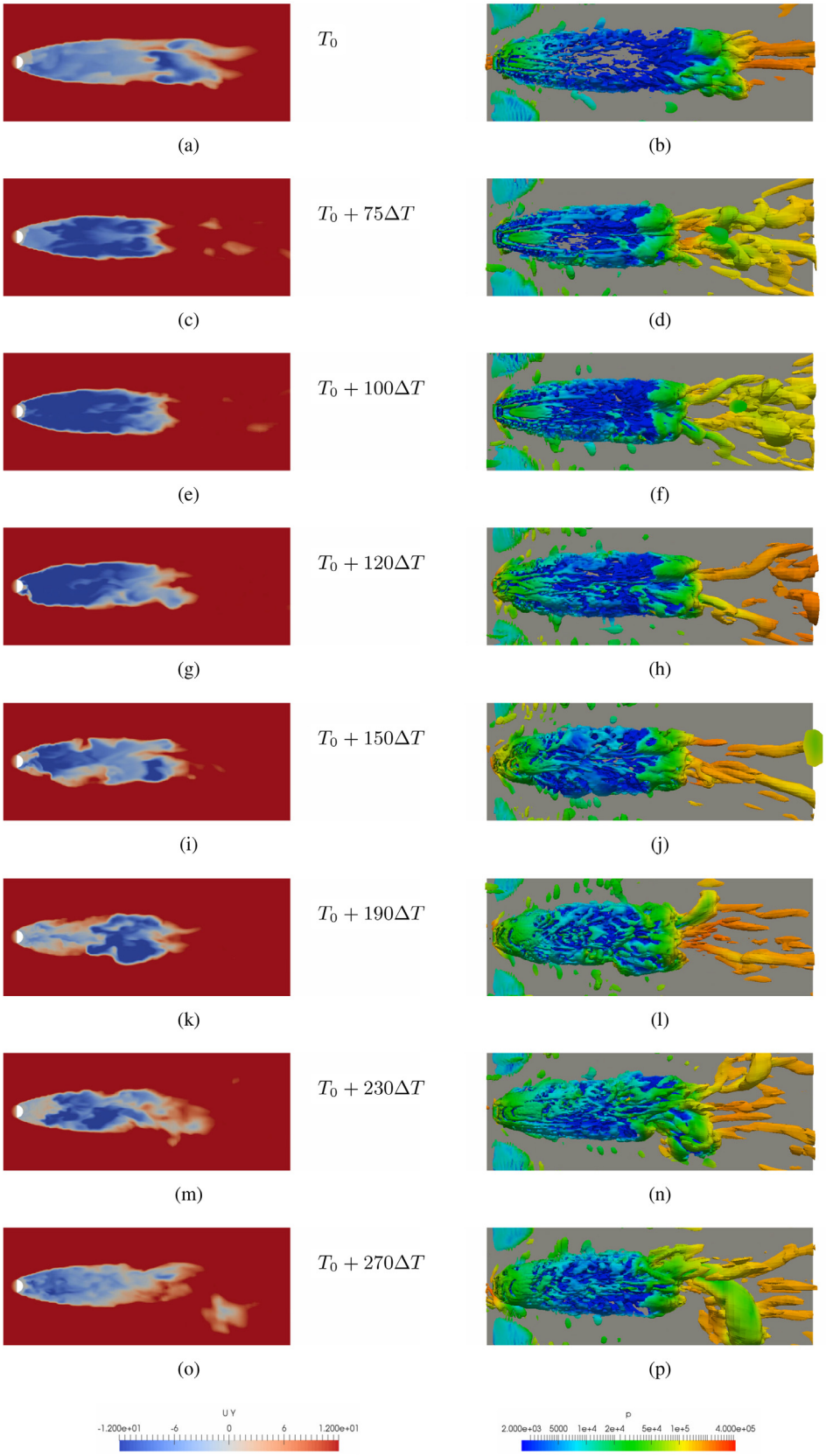

Fig. 20. Instantaneous numerical results for $\sigma = 0.641$. (a), (c), (e), (g), (i), (k), (m), (o): 2D axial velocity contours; (b), (d), (f), (h), (j), (l), (n), (p): vortical structures with $Q = 10^{6}$ s^{-2}, coloured by local pressure.

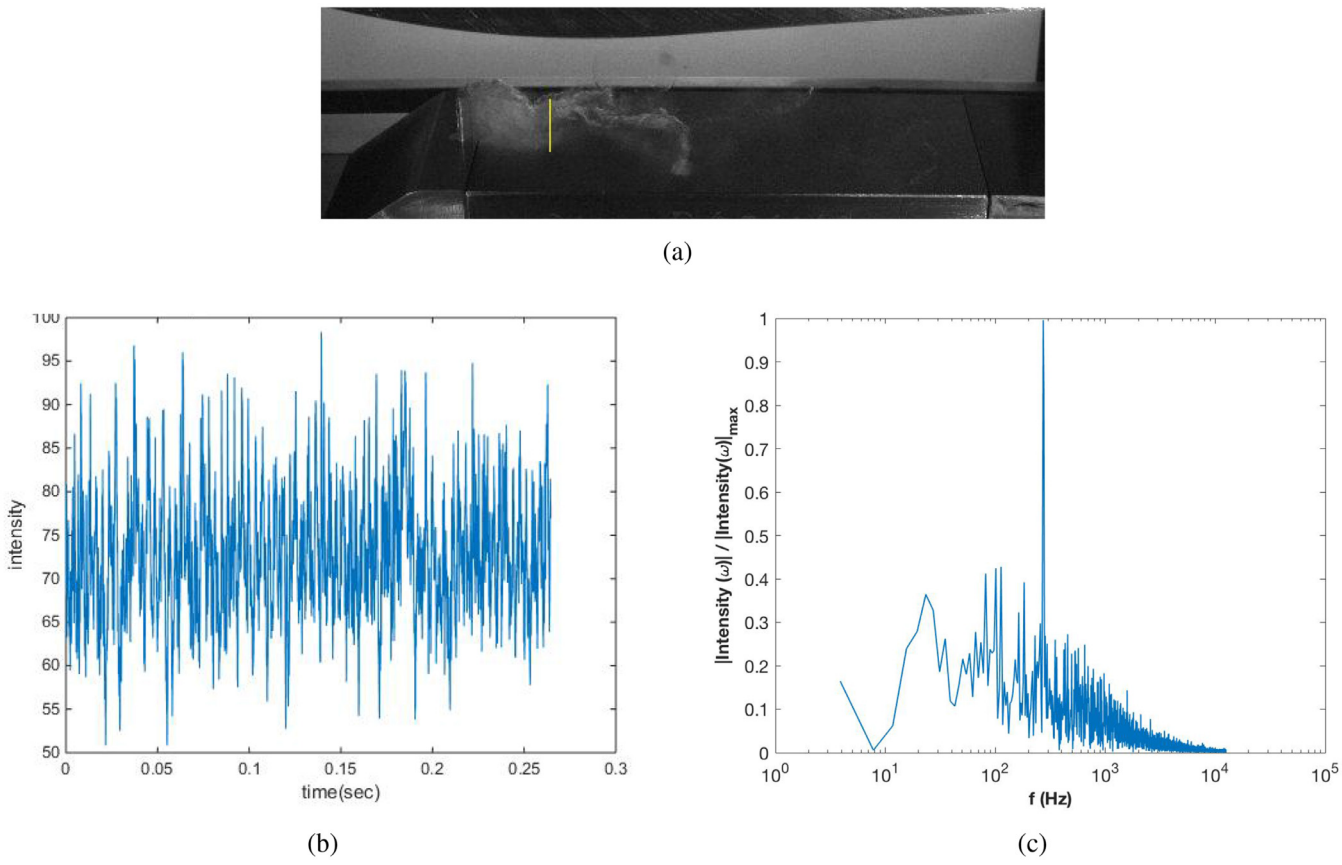

Fig. 21. (a) Time traces of the grayscale intensity for $\sigma = 0.822$; (a) measurement sample line; (b) grayscale temporal variation; (c) the normalized FFT of the signal.

vorticity in the wake area which can be expected from the deformations of the liquid-vapour interface as well. Also, the variation of pressure on the right column of Fig. 20 shows that during the whole process, the pressure inside the fixed cavity stays below the saturated vapour pressure. In fact, the cavity shedding at the tail edge as well as vorticity interactions may increase the local pressure around the end of the fixed cavity, however a large pressure wave that moves upstream and leads to a condensation shock front is not seen in the results. This is in accordance with what is stated about the experimental results, that the collapse of vapour structures and vortex interactions may cause a local pressure wave and consequent collapse of neighboring cavities, however, it does not seem to be a major source of the "high momentum" reverse flow in the fixed cavity. It is worth mentioning that in an earlier study by Ganesh et al. (2016) it was shown that in partial cavitation in the separated region forming from the apex of a wedge, a reverse condensation disturbance happens due to a shock wave that moves upwards. However, the current disturbance flow does not seem to be a shock front. In fact, as proved by Ganesh et al. (2016), over the shock front the flow pressure inside the cavity should have a sudden increase; however in the current test cases, no considerable pressure increase is seen behind the reverse flow. Besides that, a shock wave is expected to be spread freely in a whole connected vapour zone, however it can be seen in the numerical results that sometimes the disturbance jet moves only in one of the right or left sides of the fixed cavity, such as the second reverse flow in Figs. 19(n) and 20(m). Finally, due to the limitation of the homogeneous mixture model in the prediction of cavitation inception (as explained for case 3 as well), two sheet cavities are overestimated on both sides of the cylinder (which is barely seen in the experiments) and the predicted fixed cavity length (average value: 5.5 cm) is 18 % larger than the corresponding experimental one (4.6 cm). It is worth mentioning that such numerical issues are present in the results of the finer grid as well. However, the estimated pressure drop along the test rig ($p_1 - p_2$) is about 46.5 kPa which has less than 4 % difference with the corresponding experimental value (44.7 kPa, Table 2).

3.5. Cavity shedding frequency

As observed in the previous section, the cyclic, transitional, and fixed cavity patterns have different shedding behaviour. Some of the shed vortices may not be considered as cavitating and therefore the cavity shedding can have a different frequency than the vortex shedding. To find the vortex shedding frequency, in our first approach, we measured the variation of grayscale intensity over a few axial locations in the wake region. Then the dominant frequency of the obtained signal can be calculated using a fast Fourier transform (FFT). In Fig. 21, this measuring approach is demonstrated for $\sigma = 0.822$. The grayscale intensity was traced across the depicted axial location (yellow vertical line) in Fig. 21(a), and its temporal variation is plotted in Fig. 21(b). The normalized FFT of the obtained signal is shown in Fig. 21(c).

This approach can work for cyclic and transitional cavity patterns, where the detachment of cavitating vorticies is distinguishable. However, for fixed cavity pattern it is difficult to find a sample line for tracing the grayscale intensity variation, since the length of the fixed cavity varies with time and the cavity detachment location changes with time. For example, in Fig. 18, there is a considerable distance between the detachment points of the first

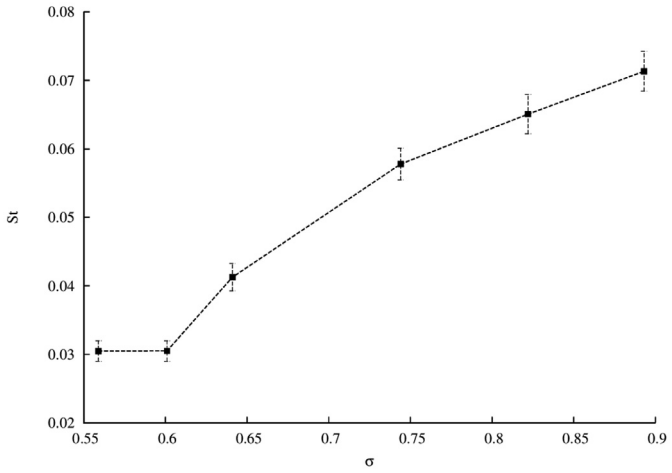

Fig. 22. Variation of the shedding frequency of cavitating vortices.

and third shedding cavities. Therefore, tracing the grayscale intensity variation can lead to erroneous results in measuring the shedding rate. For such cases ($\sigma = 0.64$, 0.60 and 0.56), the frequencies were calculated using visual inspection. For each case, the shedding rate was counted for three different time periods (10 shedding cycle in each period) and then, the averaged value was denominated to the frequency. The measurement error is estimated to be less than about 5 % for each case. Also, when this approach was compared to the first approach for cyclic and transitional cavity patterns, the difference between the two methods is about 5 % for the worst case, as shown by the error bars.

In Fig. 22, the Strouhal number (St) variation is presented as a function of the cavitation number. Here, the parameter is defined as

$$St = \frac{fD}{u_{th}}, \tag{11}$$

where f is the shedding frequency. It is seen that the non-dimensional rate of cavity shedding decreases as the flow gets more cavitating, except for the last two cases which have similar values. The Strouhal number ranges from 0.071 for $\sigma = 0.89$ to 0.0305 for $\sigma = 0.56$ and for the fixed cavity pattern it is considerably lower than the other two patterns. Furthermore, the vortex shedding Strouhal number for cyclic and transitional patterns is about 40–50% lower than the sound pressure Strouhal number ($St = 0.12$) for a semi-circular cylinder located in a uniform flow field, as reported by Yamagata et al. (2015). This difference can be due to the finite length of the cylinder as well as the effect of the bottom wall and the non-uniform upstream velocity field in the current study. In an experimental work by Park and Lee (2002), the vortex shedding frequencies for a wall-mounted finite length (circular) cylinder were measured to be between 44 to 50 Hz (equivalent to $St = 0.132$-0.15) which are 20–30 % lower than the corresponding value for a cylinder in a uniform flow field ($St = 0.19$). They also showed that the velocity boundary layer far upstream of the cylinder can affect the shedding rate and the highest value ($St = 0.15$) was measured for a uniform flow condition. It is worth mentioning that the cylinder height to diameter ratio in the current study (H/D = 1.93) is considerably lower than the one used by Park and Lee (2002) (H/D = 6), which can further influence the vortices sizes and shedding rates.

Finally, it should be mentioned that since the numerical shedding cavities may collapse too early (as explained earlier for periodic cavity pattern), sometimes smaller cavities are shed in the wake area and it is not possible to estimate the shedding frequencies of numerical simulations in the same way for experimental videos. However, for the periodic cavity pattern ($\sigma = 0.893$), the time history of average vapour fraction along a cut plane (perpendicular to main flow direction) at 12 mm behind the cylinder was measured. Based on the calculation, the α variation frequency on the left and right hand side of the wake area are 228.1 and 245.6 Hz respectively. Also, the frequency of the drag force time history is approximately $f = 270$ Hz ($St = 0.0709$) which is close to the experimental value ($St = 0.0713$). However, since the numerical frequencies are not measured in a similar way to the experimental values, we do not consider them to be comparable for validation and thus they are not added to Fig. 22.

3.6. Cavitation effect on the flow field

To investigate the effect of cavitation on the main flow behaviour and structures, the two numerical cases were simulated as non-cavitating single phase as well. Such simulations can be performed by deactivating the cavitation model and since in non-cavitating incompressible flow only the pressure differences matter, there is no need to modify the pressure values at the boundaries or in the initial condition. In Fig. 23, two instantaneous results of noncavitating flow for flow conditions equivalent to case 6 are depicted. The plots include the axial velocity contour over the same plane of Fig. 20 as well as the Q-criterion ($Q = 10^{6}$ s^{-2}) in the wake area which is coloured by local pressure. Comparing the velocity contour with the relevant plots of cavitating results (left column of Fig. 20), it can be inferred that the length and width of the wake area is considerably larger in the cavitating case. Although the fixed cavity length is sometimes overestimated in the numerical simulation, comparing the experimental results with the single-phase numerical solution yields the same conclusion. Furthermore, the Q-criterion plot shows that significantly stronger vortices are generated in the wake area of the single phase flow, especially in the recirculation zone behind the cylinder. In the cavitating flow, the vapour structures reduces the circulation, mainly

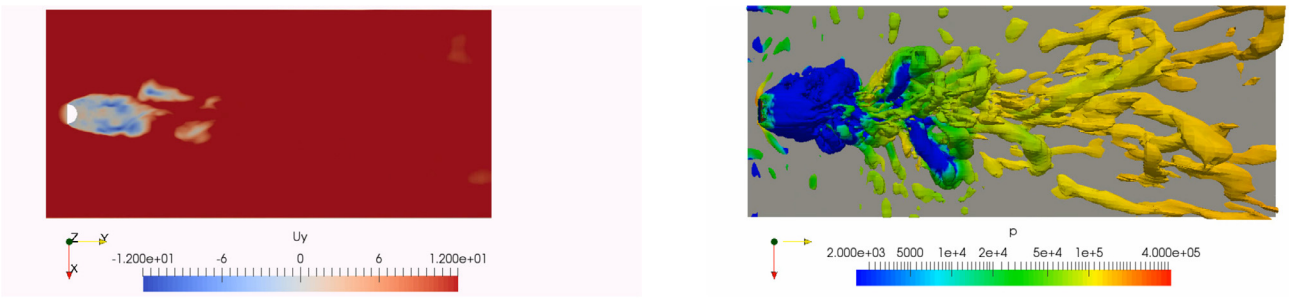

(a) (b)

Fig. 23. Non-cavitating flow results for case 6; (a) axial velocity contour; (b) vortices with $Q = 10^{6}$ s^{-2}.

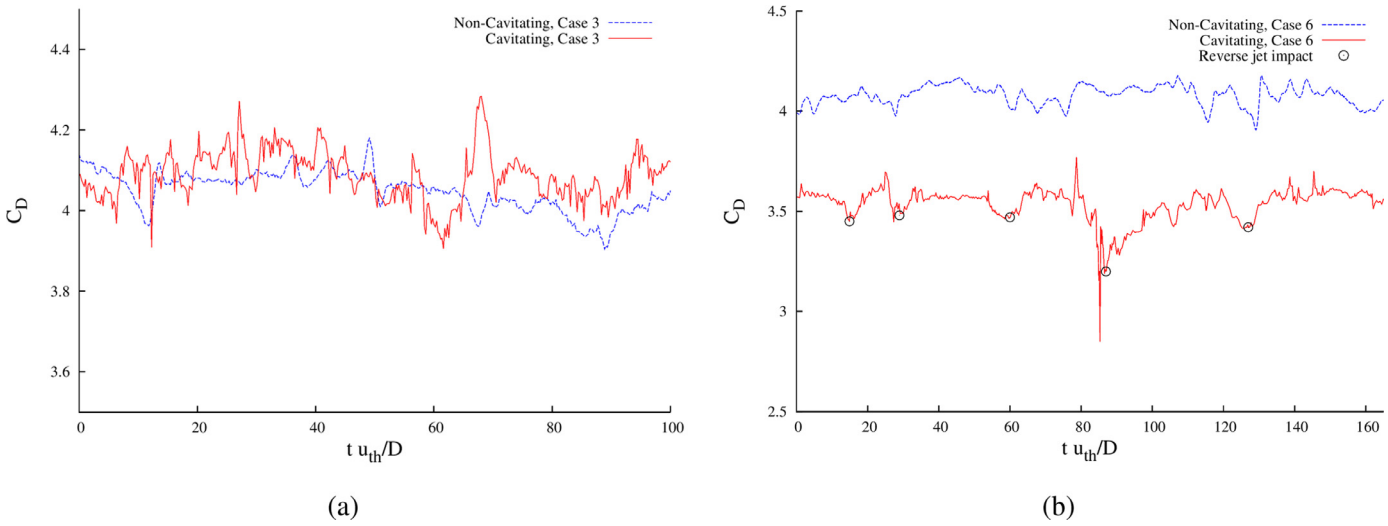

Fig. 24. Temporal variation of drag force on the bluff body: (a) case 3; (b) case 6.

in the fixed cavity part. Besides that, the pressure variation and vortex shapes are much different between the two conditions. The same effect can be seen in numerical results of case 3 as well (Fig. 11), in which the vortical structures are varied when larger cavities get weaker in the wake area, as explained earlier.

In Fig. 24 the temporal variation of the drag force coefficients for the numerical simulations are plotted. Here, the drag force is non-dimensionalized using the average velocity at the channel throat, u_{th}, and the cross sectional area of the half-circular cylinder. From this figure it is seen that for the flow conditions corresponding to case 3 (cyclic pattern), the average drag force on the cylinder and the amplitude of the variations are similar for cavitating and non-cavitating flows; however, more minor variations in the drag force are observed for the cavitating case which means that the flow has more unsteadiness. For the fixed cavity pattern ($\sigma = 0.64$), as larger cavity structures are generated in the wake area, their effect is more considerable. From Fig. 24(b), it can be seen that cavitation causes significant decrease in the drag force. Also, the stated disturbance flow further decreases the drag force on the bluff body when it hits the cylinder. The specified local minimum points in the cavitating case are related to the moments when such reverse flow reaches the cylinder. The different distances between successive minimum points show that there is no regular pattern in the occurrence of such disturbances, as stated earlier.

4. Conclusions and future works

In this study, the cavitating flow around a surface mounted semi-circular cylinder of finite length was investigated both experimentally and numerically at high Reynolds numbers ($Re = 5.6 \times 10^4 - 2.2 \times 10^5$). Also, single-phase simulations were performed to study the effect of cavitation on the flow field. Based on the observed results, the following conclusions can be drawn:

- Cavitation inception occurs along the streamwise and spanwise vortices. Contrary to earlier findings for triangular bluff bodies (e.g. Ganesh et al., 2018), the cross-streamwise (spanwise) vortices are more cavitating than the secondary streamwise vortices for the current set-up.
- By decreasing the cavitation number, other types of vortices, such as transverse vortices which start to grow at the top edge, as well as horseshoe vortices in the wake area may cavitate. As compared to earlier studies, the current tests have been performed at higher Reynolds numbers and the current set up can generate different 3D structures as the fluid passes over the top side and sharp edges of the body. Due to the interaction between primary vortices as well as the high velocity gradient in the vertical direction over the flat plate and in the wake span, secondary weaker vortices are generated in the wake area. Depending on the velocity gradient conditions such structures may get a horseshoe shape or turn into a streamwise vortex. These secondary vortices which are periodically shed downstream cannot stay as cavitating to the end of the flat plate, however at lower cavitation numbers, their vapour content collapses at larger distances from the cylinder.
- While at higher cavitation numbers, cavitating vortices are shed in a cyclic pattern in the wake area, for lower cavitation numbers, a large vapour structure is attached to the bluff body. It was found that the axial velocity component inside this fixed cavity is negative. Also, an upstream moving disturbance jet appears in the fixed cavity which accelerates the reverse flow towards the cylinder. It also affects the cavity dynamics significantly, causing its detachment from the cylinder and perturbing the liquid-vapour interface.
- The cavity shedding Strouhal number decreases by decreasing cavitation number and it is considerably lower for the fixed cavity pattern as compared to other cases.
- The vapour structures may affect the flow dynamics and vorticities considerably. For the cyclic shedding pattern, at the time instances that the vapour fraction in the wake area is larger, the flow vorticity is smaller as compared to other instances with lower vapour content. Also, for the fixed cavity pattern, the vapour structures significantly modify the vorticity and shape of the vortical structures, as well as their shedding pattern in the wake area.
- The comparison between the single-phase flow and cavitating flow simulations show that at lower cavitation numbers with fixed cavity pattern, the drag force on the cylinder is reduced and the temporal plot of the drag force has local minimum at the instances when the disturbance jet hits the bluff body.

Also, it was observed that the semi-circular bluff body can induce localised cavity patterns and the flow can become quite erosive, depending on the flow conditions. Since the observed shed cavities have various sizes and collapse rates, it is expected that the surface erosion pattern varies for different cases. In a fu-

ture study, the erosion behaviour of this flow for different conditions will be investigated. In addition, numerical simulations were shown to be a suitable tool for further understanding and analysis of the experimental tests. However, in this study, the homogeneous mixture model, which is widely used for large scale applications, was limited in the prediction of cavitation inception as well as the length of fixed cavities. In future, a hybrid Eulerian mixture - Lagrangian bubble model will be utilized for numerical modelling which is supposed to have improved accuracy in the estimation of cavitation inception and collapse rate. Therefore, it will be possible to have more quantitative agreement between numerical results and experimental data and more flow details can reliably be studied based of CFD results. One of the possible feature to investigate further is the interaction between cavitation and flow vortices. Also the effect of turbulence can be studied using CFD results. In this study, high speed visualization was not a suitable tool to measure flow turbulence and it was assumed that the average flow pattern does not vary considerably in the range $Re = 7.4 \times 10^4 - 21.5 \times 10^4$. As stated earlier, such an assumption can be verified from similar average drag coefficients of non-cavitating flows which are approximately equal to 4 for both cases in Fig. 24.

Acknowledgments

This work is funded through the EU H2020 project CaFE, a Marie Skłodowska-Curie Action Innovative Training Network project, grant number 642536. The authors wish to express their gratitude to Dr. Etienne Parkinson and Dr. Jean-Christophe Marongiu and all laboratory technicians and researchers at Andritz Hydro (Switzerland) for hosting Ebrahim Ghahramani and Saad Jahangir in a two-month study visit as a part of the CaFE project. We specially thank Hélène Garcin, who kindly shared the numerical geometry for simulation. The computations were performed on resources at Chalmers Centre for Computational Sciences and Engineering (C3SE) provided by the Swedish National Infrastructure for Computing (SNIC).

Supplementary materials

Supplementary material associated with this article can be found, in the online version, at doi:10.1016/j.ijmultiphaseflow.2019.103191.

References

Adair, A., Mastikhin, I.V., Newling, B., 2018. Motion-sensitized sprite measurements of hydrodynamic cavitation in fast pipe flow. Magn. Reson. Imaging 49, 71–77.
Asnaghi, A., Feymark, A., Bensow, R., 2017. Improvement of cavitation mass transfer modeling based on local flow properties. Int. J. Multiphase Flow 93, 142–157.
Asnaghi, A., Feymark, A., Bensow, R.E., 2015. Computational analysis of cavitating marine propeller performance using openfoam. In: Proceedings of Second Workshop on Cavitation and Propeller Performance, the Fourth International Symposium on Marine Propulsors, SMP.
Asnaghi, A., Svennberg, U., Bensow, R.E., 2018. Numerical and experimental analysis of cavitation inception behaviour for high-skewed low-noise propellers. Appl. Ocean Res. 79, 197–214.
Avellan, F., Dupont, P., Farhat, M., 1991. Cavitation erosion power. In: 1st ASME-JSME Fluid Engineering Conference, Portland, OR, June, pp. 23–27.
Balas, G.J., Bokor, J., Vanek, B., Arndt, R.E., 2006. Control of High-speed Underwater Vehicles. In: Control of Uncertain Systems: Modelling, Approximation, and Design. Springer, pp. 25–44.
Barton, I.E., 1998. Comparison of simple-and piso-type algorithms for transient flows. Int. J. Numer. Methods Fluids 26 (4), 459–483.
Belahadji, B., Franc, J.-P., Michel, J.-M., 1995. Cavitation in the rotational structures of a turbulent wake. J. Fluid Mech. 287, 383–403.
Bensow, R.E., Bark, G., 2010. Implicit les predictions of the cavitating flow on a propeller. J. Fluids Eng. 132 (4), 41302.
Brandner, P., Walker, G., Niekamp, P., Anderson, B., 2010. An experimental investigation of cloud cavitation about a sphere. J. Fluid Mech. 656, 147–176.
Chang, N.A., Choi, J., Yakushiji, R., Ceccio, S.L., 2012. Cavitation inception during the interaction of a pair of counter-rotating vortices. Phys. Fluids 24 (1), 14107.
Dash, A., Jahangir, S., Poelma, C., 2018. Direct comparison of shadowgraphy and x-ray imaging for void fraction determination. Meas. Sci. Technol. 29 (12), 125303.
Drikakis, D., Hahn, M., Mosedale, A., Thornber, B., 2009. Large eddy simulation using high-resolution and high-order methods. Philos. Trans. R. Soc. A: Math. Phys. Eng. Sci. 367 (1899), 2985–2997.
Escaler, X., Avellan, F., Egusquiza, E., 2001. Cavitation erosion prediction from inferred forces using material resistance data. http://resolver.caltech.edu/cav2001:sessionA3.005.
Escaler, X., Farhat, M., Avellan, F., Egusquiza, E., 2003. Cavitation erosion tests on a 2d hydrofoil using surface-mounted obstacles. Wear 254 (5–6), 441–449.
Eskilsson, C., Bensow, R., 2012. A compressible model for cavitating flow: comparison between euler, rans and les simulations. 29th Symposium on Naval Hydrodynamics, Gothenburg, Sweden.
Foeth, E.-J., van Terwisga, T., van Doorne, C., 2008. On the collapse structure of an attached cavity on a three-dimensional hydrofoil. J. Fluids Eng. 130 (7), 71303.
Franc, J.-P., Michel, J.-M., 2006. Fundamentals of Cavitation, 76. Springer Science & Business Media.
Fry, S., 1984. Investigating cavity/wake dynamics for a circular cylinder by measuring noise spectra. J. Fluid Mech. 142, 187–200.
Ganesh, H., Deijlen, L., Bhatt, A., Wu, J., Ceccio, S.L., 2018. Cavitation dynamics in wakes of bluff bodies. 32nd Symposium on Naval Hydrodynamics. Hamburg, Germany 5–10 August 2018.
Ganesh, H., Mäkiharju, S.A., Ceccio, S.L., 2016. Bubbly shock propagation as a mechanism for sheet-to-cloud transition of partial cavities. J. Fluid Mech. 802, 37–78.
Ghahramani, E., Arabnejad, M.H., Bensow, R.E., 2018. Realizability improvements to a hybrid mixture-bubble model for simulation of cavitating flows. Comput. Fluids 174, 135–143.
Ghahramani, E., Arabnejad, M.H., Bensow, R.E., 2019. A comparative study between numerical methods in simulation of cavitating bubbles. Int. J. Multiphase Flow 111, 339–359.
Gnanaskandan, A., Mahesh, K., 2016. Numerical investigation of near-wake characteristics of cavitating flow over a circular cylinder. J. Fluid Mech. 790, 453–491.
Habchi, C., Gillet, N., Velghe, A., Bohbot, J., Schmid, A., Von Rotz, B., Herrmann, K., 2014. On the role of cavitation in marine large diesel injector: numerical investigation of nozzle orifices eccentricity. In: ILASS-Europe 2014, 26th Annual Conference on Liquid Atomization and Spray Systems.
Ibsen, S., Schutt, C.E., Esener, S., 2013. Microbubble-mediated ultrasound therapy: a review of its potential in cancer treatment. Drug Des. Dev. Ther. 7, 375.
Jahangir, S., Hogendoorn, W., Poelma, C., 2018. Dynamics of partial cavitation in an axisymmetric converging-diverging nozzle. Int. J. Multiphase Flow 106, 34–45.
Jahangir, S., Wagner, E.C., Mudde, R.F., Poelma, C., 2019. Void fraction measurements in partial cavitation regimes by x-ray computed tomography. Int. J. Multiphase Flow 120, 103085.
Kumar, P., Chatterjee, D., Bakshi, S., 2017. Experimental investigation of cavitating structures in the near wake of a cylinder. Int. J. Multiphase Flow 89, 207–217.
Kumar, P., Dhiman, C., Bakshi, S., 2018. Numerical study of cavitating structure near wake of a circular cylinder. Tenth International Symposium on Cavitation (CAV2003). Citeseer.
Matsudaira, Y., Gomi, Y., Oba, R., 1992. Characteristics of bubble-collapse pressures in a karman-vortex cavity. JSME international journal. Ser. 2, Fluids engineering, heat transfer, power, combustion, thermophysical properties 35 (2), 179–185.
Mitroglou, N., Lorenzi, M., Santini, M., Gavaises, M., 2016. Application of x-ray micro-computed tomography on high-speed cavitating diesel fuel flows. Exp. Fluids 57 (11), 175.
OpenFoam, 2013. The OpenFOAM foundation. http://openfoam.org/version/2-2-2/.
Park, C.-W., Lee, S.-J., 2002. Flow structure around a finite circular cylinder embedded in various atmospheric boundary layers. Fluid Dyn. Res. 30 (4), 197.
Patankar, S.V., Spalding, D.B., 1983. A Calculation Procedure for Heat, Mass and Momentum Transfer in Three-dimensional Parabolic Flows. In: Numerical Prediction of Flow, Heat Transfer, Turbulence and Combustion. Elsevier, pp. 54–73.
Rao, B.S., Chandrasekhara, D., 1976. Some characteristics of cavity flow past cylindrical inducers in a venturi. J. Fluids Eng. 98 (3), 461–466.
Saito, Y., Sato, K., 2003. Cavitation bubble collapse and impact in the wake of a circular cylinder. Fifth International Symposium on Cavitation (CAV2003). Citeseer.
Schenke, S., van Terwisga, T.J., 2019. An energy conservative method to predict the erosive aggressiveness of collapsing cavitating structures and cavitating flows from numerical simulations. Int. J. Multiphase Flow 111, 200–218.
Schnerr, G.H., Sauer, J., 2001. Physical and numerical modeling of unsteady cavitation dynamics. Fourth international conference on multiphase flow, New Orleans, USA, 1.
Schnerr, G.H., Sezal, I.H., Schmidt, S.J., 2008. Numerical investigation of three-dimensional cloud cavitation with special emphasis on collapse induced shock dynamics. Phys. Fluids 20 (4), 40703.
Seo, J.H., Moon, Y.J., Shin, B.R., 2008. Prediction of cavitating flow noise by direct numerical simulation. J. Comput. Phys. 227 (13), 6511–6531.
Singhal, A.K., Athavale, M.M., Li, H., Jiang, Y., 2002. Mathematical basis and validation of the full cavitation model. Trans.-Am. Soc. Mech.Eng. J. Fluids Eng. 124 (3), 617–624.
Tulin, M.P., 1963. Supercavitating flows-small perturbation theory. Technical Report. Hydronautics Inc Laurel MD.
Van Terwisga, T., 2009. Cavitation erosion-a review of physical mechanisms and erosion risk models. CAV2009.
Wang, Z., Huang, B., Zhang, M., Wang, G., Zhao, X., 2018. Experimental and numerical investigation of ventilated cavitating flow structures with special emphasis on vortex shedding dynamics. Int. J. Multiphase Flow 98, 79–95.
Yamagata, T., Saito, N., Fujisawa, N., 2015. Aeolian tone from a semi-circular cylinder in a stream. J. Flow Control Meas.Visualization 4 (1), 30.
Young, J., Holl, J.W., 1966. Effects of cavitation on periodic wakes behind symmetric wedges. J. Basic Eng. 88 (1), 163–176.